

## Stardust Interstellar Preliminary Examination IV: Scanning transmission X-ray microscopy analyses of impact features in the Stardust Interstellar Dust Collector

Anna L. BUTTERWORTH<sup>1\*</sup>, Andrew J. WESTPHAL<sup>1</sup>, Tolek TYLISZCZAK<sup>2</sup>, Zack GAINSFORTH<sup>1</sup>, Julien STODOLNA<sup>1</sup>, David R. FRANK<sup>3</sup>, Carlton ALLEN<sup>4</sup>, David ANDERSON<sup>1</sup>, Asna ANSARI<sup>5</sup>, Saša BAJT<sup>6</sup>, Ron K. BASTIEN<sup>3</sup>, Nabil BASSIM<sup>7</sup>, Hans A. BECHTEL<sup>2</sup>, Janet BORG<sup>8</sup>, Frank E. BRENNER<sup>9</sup>, John BRIDGES<sup>10</sup>, Donald E. BROWNLEE<sup>11</sup>, Mark BURCHELL<sup>12</sup>, Manfred BURGHAMMER<sup>13</sup>, Hitesh CHANGELA<sup>14</sup>, Peter CLOETENS<sup>13</sup>, Andrew M. DAVIS<sup>15</sup>, Ryan DOLL<sup>16</sup>, Christine FLOSS<sup>16</sup>, George FLYNN<sup>17</sup>, Eberhard GRÜN<sup>18</sup>, Philipp R. HECK<sup>5</sup>, Jon K. HILLIER<sup>19</sup>, Peter HOPPE<sup>20</sup>, Bruce HUDSON<sup>21</sup>, Joachim HUTH<sup>20</sup>, Brit HVIDE<sup>5</sup>, Anton KEARSLEY<sup>22</sup>, Ashley J. KING<sup>15</sup>, Barry LAI<sup>23</sup>, Jan LEITNER<sup>20</sup>, Laurence LEMELLE<sup>24</sup>, Hugues LEROUX<sup>25</sup>, Ariel LEONARD<sup>16</sup>, Robert LETTIERI<sup>1</sup>, William MARCHANT<sup>1</sup>, Larry R. NITTLER<sup>26</sup>, Ryan OGLIORE<sup>27</sup>, Wei Ja ONG<sup>16</sup>, Frank POSTBERG<sup>19</sup>, Mark C. PRICE<sup>12</sup>, Scott A. SANDFORD<sup>28</sup>, Juan-Angel San̄s TRESSERAS<sup>13</sup>, Sylvia SCHMITZ<sup>9</sup>, Tom SCHOONJANS<sup>29</sup>, Geert SILVERSMIT<sup>29</sup>, Alexandre S. SIMIONOVICI<sup>30</sup>, Vicente A. SOLÉ<sup>13</sup>, Ralf SRAMA<sup>31</sup>, Frank J. STADERMANN<sup>16</sup>, Thomas STEPHAN<sup>15</sup>, Veerle J. STERKEN<sup>18,31,32</sup>, Rhonda M. STROUD<sup>7</sup>, Steven SUTTON<sup>23</sup>, Mario TRIELOFF<sup>19</sup>, Peter TSOU<sup>33</sup>, Akira TSUCHIYAMA<sup>34</sup>, Bart VEKEMANS<sup>29</sup>, Laszlo VINCZE<sup>29</sup>, Joshua VON KORFF<sup>1</sup>, Naomi WORDSWORTH<sup>35</sup>, Daniel ZEVIN<sup>1</sup>, Michael E. ZOLENSKY<sup>4</sup>, and > 30,000 Stardust@home dusters<sup>36</sup>

<sup>1</sup>Space Sciences Laboratory, University of California, Berkeley, California, USA

<sup>2</sup>Advanced Light Source, Lawrence Berkeley National Laboratory, Berkeley, California, USA

<sup>3</sup>ESCG, NASA JSC, Houston, Texas, USA

<sup>4</sup>ARES, NASA JSC, Houston, Texas, USA

<sup>5</sup>Robert A. Pritzker Center for Meteoritics and Polar Studies, The Field Museum of Natural History, Chicago, Illinois, USA

<sup>6</sup>Deutsches Elektronen-Synchrotron, Hamburg, Germany

<sup>7</sup>Materials Science and Technology Division, Naval Research Laboratory, Washington, District of Columbia, USA

<sup>8</sup>Institut d'Astrophysique Spatiale, Orsay, France

<sup>9</sup>Geoscience Institute, Goethe University Frankfurt, Frankfurt, Germany

<sup>10</sup>Space Research Centre, University of Leicester, Leicester, UK

<sup>11</sup>Department of Astronomy, University of Washington, Seattle, Washington, USA

<sup>12</sup>University of Kent, Canterbury, Kent, UK

<sup>13</sup>European Synchrotron Radiation Facility, Grenoble, France

<sup>14</sup>George Washington University, Washington, District of Columbia, USA

<sup>15</sup>Department of the Geophysical Sciences, University of Chicago, Chicago, Illinois, USA

<sup>16</sup>Department of Physics, Washington University, St. Louis, Missouri, USA

<sup>17</sup>Department of Physics, State University of New York at Plattsburgh, Plattsburgh, New York, USA

<sup>18</sup>Max-Planck-Institut für Kernphysik, Heidelberg, Germany

<sup>19</sup>Institut für Geowissenschaften, Universität Heidelberg, Heidelberg, Germany

<sup>20</sup>Max-Planck-Institut für Chemie, Mainz, Germany

<sup>21</sup>Midland, Ontario, Canada

<sup>22</sup>Natural History Museum, London, UK

<sup>23</sup>Advanced Photon Source, Argonne National Laboratory, Chicago, Illinois, USA

<sup>24</sup>Ecole Normale Supérieure de Lyon, Lyon, France

<sup>25</sup>University Lille, Lille, France

<sup>26</sup>Carnegie Institution of Washington, Washington, District of Columbia, USA

<sup>27</sup>University of Hawai'i at Manoa, Honolulu, Hawai'i, USA

<sup>28</sup>NASA Ames Research Center, Moffett Field, California, USA

<sup>29</sup>University of Ghent, Ghent, Belgium<sup>30</sup>Institut des Sciences de la Terre, Observatoire des Sciences de l'Univers de Grenoble, Grenoble, France<sup>31</sup>Institut für Raumfahrtssysteme, Universität Stuttgart, Stuttgart, Germany<sup>32</sup>Institut für Geophysik und Extraterrestrische Physik, Technische Universität Braunschweig, Braunschweig, Germany<sup>33</sup>Jet Propulsion Laboratory, Pasadena, California, USA<sup>34</sup>Osaka University, Osaka, Japan<sup>35</sup>South Buckinghamshire, UK<sup>36</sup>Worldwide

\*Corresponding author. E-mail: annab@ssl.berkeley.edu

*(Received 19 December 2012; revision accepted 16 August 2013)*


---

**Abstract**—We report the quantitative characterization by synchrotron soft X-ray spectroscopy of 31 potential impact features in the aerogel capture medium of the Stardust Interstellar Dust Collector. Samples were analyzed in aerogel by acquiring high spatial resolution maps and high energy-resolution spectra of major rock-forming elements Mg, Al, Si, Fe, and others. We developed diagnostic screening tests to reject spacecraft secondary ejecta and terrestrial contaminants from further consideration as interstellar dust candidates. The results support an extraterrestrial origin for three interstellar candidates: I1043,1,30 (Orion) is a 3 pg particle with Mg-spinel, forsterite, and an iron-bearing phase. I1047,1,34 (Hylabrook) is a 4 pg particle comprising an olivine core surrounded by low-density, amorphous Mg-silicate and amorphous Fe, Cr, and Mn phases. I1003,1,40 (Sorok) has the track morphology of a high-speed impact, but contains no detectable residue that is convincingly distinguishable from the background aerogel. Twenty-two samples with an anthropogenic origin were rejected, including four secondary ejecta from impacts on the Stardust spacecraft aft solar panels, nine ejecta from secondary impacts on the Stardust Sample Return Capsule, and nine contaminants lacking evidence of an impact. Other samples in the collection included I1029,1,6, which contained surviving solar system impactor material. Four samples remained ambiguous: I1006,2,18, I1044,2,32, and I1092,2,38 were too dense for analysis, and we did not detect an intact projectile in I1044,3,33. We detected no radiation effects from the synchrotron soft X-ray analyses; however, we recorded the effects of synchrotron hard X-ray radiation on I1043,1,30 and I1047,1,34.

---

## INTRODUCTION

NASA's Stardust mission successfully returned its sample return capsule (SRC) to Earth in a spectacular  $12 \text{ km s}^{-1}$  re-entry, parachute descent and safe landing at the Utah Test and Training Range in 2006. The SRC contained two collectors: the cometary collector is an approximately  $1039 \text{ cm}^2$  array of silica aerogel tiles and aluminum foils containing impacts from comet 81P/Wild 2. The Stardust Interstellar Dust Collector (SIDC) was a second aft-facing array of similar aerogel tiles and Al foils, which had been exposed to the interstellar dust stream for 195 days during the cruise phase of the spacecraft's journey to comet Wild 2. The SIDC may contain the first samples of contemporary interstellar dust ever returned to Earth. Presolar grains found in meteorites predate the 4.6 Ga old solar system; local interstellar dust is likely to be <400 Myr old (e.g., Jones

et al. 1996), so the Stardust SIDC collection may contain a contemporary sample of the galactic environment.

We formed a consortium in 2008 to conduct the Interstellar Preliminary Examination (ISPE). The goal was to characterize the SIDC collection to provide investigators with the information needed to make future sample requests (Westphal et al. 2014a). The ISPE was limited to identifying candidates of interstellar dust in the SIDC by a combination of efforts including locating possible impacts in the aerogel collector or aluminum foils, measuring track trajectories, and analyzing the composition of impactors—in aerogel—to rule out anthropogenic sources such as secondary ejecta from the Stardust spacecraft. Primary extraterrestrial impacts from within the solar system could be identified by their trajectory, but isotope measurements, which are likely to be diagnostic of extra solar system origin, were not permitted during ISPE.

We expected any collected interstellar dust to be much smaller (submicrometer size range) and much rarer than the Stardust cometary impactors. As a result, we developed an online search called Stardust@home (Westphal et al. 2014b), which has recruited more than 30,000 volunteers to search optical microscope images of the SIDC aerogel for possible impact tracks. The project resulted in the discovery of 70 tracks.

Frank et al. (2013) describe the development of aerogel extractions optimized for nondestructive characterization of tracks and particles remaining in the aerogel capture medium. At the time of this writing, no sufficiently low-risk method exists for extracting submicrometer-sized particles from aerogel for subsequent sample preparation for electron microscopy or mass spectrometry. These techniques were therefore excluded from ISPE, which instead focused on preliminary characterizations that could be performed in small volumes of aerogel containing a single impact track feature. (Note that, in contrast, electron microscopy was a key ISPE technique for analysis of impact features in Al foils; Stroud et al. 2014.) The goal of characterization was to reject background contamination in the SIDC collection from further consideration as candidates for interstellar dust, particularly where trajectory information was ambiguous. The ISPE characterization effort involved coordinated X-ray analyses using four techniques on seven beamlines at four synchrotron facilities: in this volume, Bechtel et al. (2014) report infrared spectroscopic analysis; Brenker et al. (2014), Flynn et al. (2014), and Simionovici et al. (2014) report X-ray fluorescence spectroscopic analyses; Gainsforth et al. (2014) report X-ray diffraction analyses; and, in this work, we provide an account of the scanning transmission X-ray microscopy (STXM), including X-ray absorption spectroscopic analyses of 31 samples extracted from the SIDC.

Also reported in this volume are analyses of laboratory hypervelocity impact experiments with analogs into aerogel to understand high-speed track morphologies and better inform searching strategies in Stardust@home (Postberg et al. 2014); Sterken et al. (2014) predicted dust flux and trajectories based on Stardust flight information and dust propagation models; finally, a parallel ISPE effort to search and analyze impact craters in the Al foils, which separated aerogel tiles in the SIDC, is described by Stroud et al. (2014).

## METHODS

Candidate impact features were identified through Stardust@home (Westphal et al. 2014b). Samples were prepared at NASA Johnson Space Center, Houston

(JSC), described in Frank et al. (2013). Small volumes of aerogel containing a candidate impact feature were extracted using the keystone technique (Westphal et al. 2004). Most samples produced for ISPE were picokeystones, whose modified keystone design included thinner aerogel (60–150  $\mu\text{m}$ ) around the feature of interest, allowing for STXM analysis, supported by a thicker bulk keystone (430  $\mu\text{m}$ ). The picokeystones were sandwiched between two back-to-back 50 nm or 70 nm thick silicon nitride membranes on 200  $\mu\text{m}$  thick silicon frames (Norcada), and the resulting 400  $\mu\text{m}$  thick sandwich was affixed to an aluminum mount. Because aerogel is elastic, the keystones were held in place under gentle compression by the silicon nitride membranes.

Each Stardust@home volunteer who first identified a particular feature, which was subsequently extracted from the SIDC, was given the opportunity to name the sample. We refer to each ISPE sample by its JSC-assigned curation number, its shorthand track number, and by the Stardust@home alias, if one exists.

The analyses described in this work were performed at the STXM beamline 11.0.2, located on a 5 cm period elliptical polarization undulator at the Advanced Light Source (ALS), Lawrence Berkeley National Laboratory, (Tyliczszak et al. 2004). A variable-included-angle plane-grating monochromator provided a resolving power  $E/\Delta E \geq 3000$  in the energy range 80–2000 eV. X-ray absorption near-edge structure (XANES) spectral acquisitions achieve 60 meV resolution at the C K-edge and 200 meV resolution at the Al K-edge. We used a Fresnel zone plate (manufactured by the Center for X-ray Optics [CXRO], LBNL; Olynick et al. 2004) to focus monochromatic X-rays to a 30 nm beamspot. We also used, on one occasion, ALS beamline 5.3.2.1, which is situated on a bending magnet and has a spherical grating monochromator with energy range of 600–2600 eV. Flux at both beamlines was optimized to 10–15 MHz for single photon counting acquisition

## Scanning Transmission X-ray Microscopy

Scanning transmission X-ray microscopy may be used to measure the absorption of soft X-rays transmitted through a material by normalizing the measured photon count intensity ( $I$ ), with respect to background photon count ( $I_0$ ) at an energy, such that

$$I = I_0 e^{-\mu \rho d} \quad (1)$$

where  $\mu$  is the absorption cross section, at that energy,  $\rho$  is the (total) density in  $\text{g cm}^{-3}$ , and  $d$  is the thickness of material. We used values for  $\mu$  tabulated by Lawrence Berkeley National Laboratory's Center for X-Ray Optics (CXRO, [http://henke.lbl.gov/optical\\_](http://henke.lbl.gov/optical_)

constants/). Optical density (OD) is the fraction of absorbed radiation at a given energy:

$$\text{OD} = -\ln(I/I_0) = \mu\rho d. \quad (2)$$

The column density of an element may thus be determined by measuring the difference in OD ( $\Delta\text{OD}$ ) across an element's absorption edge, or "edge jump."

$$\Delta\text{OD} = \Delta\mu(\rho d) = \Delta\mu\sigma \quad (3)$$

where  $\Delta\mu$  is the difference in absorption coefficient across the absorption edge, and  $\rho$ ,  $d$  are the density and thickness of that element, respectively. In practice, the postedge OD spectrum is extrapolated back to the absorption edge, ignoring near-edge (XANES) resonance peaks. The fitted pre-edge spectrum is then subtracted to give  $\Delta\text{OD}$ . Working with samples of unknown thickness, like projectiles captured in aerogel (as opposed to ultramicrotomed thin sections of uniform thickness), it is usually possible only to compute column density,  $\sigma$ , and not to resolve density and thickness. The mass of an element ( $m$ ) within a given area (e.g., a particle in a stack map) can be computed from

$$m = \langle\sigma\rangle A \quad (4)$$

where  $\langle\sigma\rangle$  is the average value of  $\sigma$  and  $A$  is the projected area of the particle in the map.

We used the following procedure for the quantification of elemental masses:

1. Acquire a stack—several images taken at discrete energies spanning the absorption edge, or just two images (one pre-edge, one postedge) to make a map.
2. Align the stack (correct for position drift) using an automated alignment algorithm (Zimba, compiled within the STXM analysis IDL software suite aXis2000; <http://unicorn.mcmaster.ca/aXis2000.html>).
3. Using a region well separated from the particle, measure the background aerogel absorption ( $I_0$ ) at each energy.
4. Using Equation 2 and the background aerogel  $I_0$  spectrum, calculate the OD spectrum,  $I$ , at each pixel.
5. Sum the average spectra in the region of the particle.
6. Separately fit the pre-edge and postedge regions to a straight line, ignoring any large resonance peaks close to the edge, extrapolate both fit lines to the edge, and measure the edge jump  $\Delta\text{OD}$ ; or, in the case of two-energy maps, we measure  $\Delta\text{OD}$  and

factor in a resonance enhancement for that element and phase.

7. Calculate the mass of the analyzed element contained within each pixel using  $m = (\Delta\text{ODA}/\Delta\mu)$ , where  $\Delta\mu$  is the tabulated pre-edge subtracted cross section; or calculate the mass for an area using Equation 4.

Systematic errors generally dominate over statistical (photon counting) errors in the error budget for STXM quantification, unless the concentrations are very near the detection threshold. They result from:

1. Uncertainties in tabulated cross sections (generally  $<10\%$ ). We have not included these systematic errors in our analyses, but assume that the CXRO cross sections are correct.
2. Uncertainties in resonance amplitudes near the edge, only in the case of maps in which the full spectrum is not sampled (a factor of 2–5 for Mg and Al, a factor up to 10 for Fe).
3. "Bleed over" of the spatial tails of the beam in strongly absorbing samples with strong absorption contrast leads to a systematic underestimate of mass. We measured this effect to be  $<5\%$  for picokeystones at the Fe L-edge for  $\text{OD} < 2.9$  ( $>5\%$  transmission), but the effect was much larger (800% Fe underestimation) at  $\text{OD} = 3.2$  (4% transmission).

### Sensitivity

Scanning transmission X-ray microscopy detection limits for common geological elements lie in the range 3–20 fg  $\mu\text{m}^{-2}$ , based on elements' edge jumps,  $\Delta\text{OD}$  (Equation 3). In practice, the detection sensitivity depends on background noise, which affects normalization (Equation 2). Detection thresholds can be improved by mapping at near-edge resonance peaks, which boosts signal/noise at the cost of increased systematic errors in quantification.

Advanced Light Source STXM 11.0.2 is routinely used for quantification of percent-level concentrations. In comparison, the hard X-ray synchrotron fluorescence and diffraction beamlines involved in the ISPE detect trace concentrations of elements in aerogel: 2-ID-D at the Advanced Photon Source and ID-22 at the European Synchrotron Radiation Facility (ESRF) detect  $Z \geq 20$  (Ca) and ID-13 at ESRF detects  $Z \geq 14$  (Si). STXM and XRF beamlines overlap for the transition metals, which enables overall normalization through measurements of the abundance of Fe.

### Energy Calibration

We acquired a number of spectra from common minerals found in meteorites at the Mg, Al, and Si



K-edges and Fe L<sub>23</sub>-edge, to build a high energy-resolution spectrum library for comparison with samples from the SIDC. All of the standard spectra used in this work were acquired at beamline ALS 11.0.2 STXM and compared with literature spectra, where available, for energy calibration.

Mg K-edge XANES (1300 to 1350 eV) are routinely calibrated using Ne (867.3 eV) and Al metal (1559 eV). Without further calibration against a Mg standard, absolute energy uncertainties are smaller than 1.5 eV. The relative energy determination of a given measurement within a spectrum is much better, approximately 0.2 eV, in this energy region. We typically took spectra with 0.2 eV energy steps across the Mg K-edge. For energy calibration refinement, we matched the position of the first peak in our periclase spectrum to 1311.3 eV, after Li et al. (1999).

Al spectra acquisitions, typically 0.2 eV steps across the Al K-edge, were energy calibrated against Al metal (at 1559 eV) and published spectra (Ildefonse et al. 1998; Marcelli et al. 2000; Neuville et al. 2009).

Fe L-edge lies within a well-calibrated energy range, wherein absolute energies are correct to within 80 meV (using CO<sub>2</sub>, N<sub>2</sub>, and Ne calibrants). Si K-edge standards were calibrated against Si metal (1839.2 eV); otherwise, energy accuracy in this energy range is approximately 2 eV.

### Limiting Photon Dose

Due to higher cross sections at lower energies, soft X-rays have the potential to efficiently interact and alter material resulting in radiation damage; the effects on C are well documented (e.g., Wang et al. 2009). We took steps to minimize risk to the samples (Butterworth et al. 2008). The ISPE team mandated that X-ray fluence for all synchrotron analyses should not exceed the fluence the particles experienced while resident in interstellar space, based on values from Gruber et al. (1999). This fluence limit was energy-dependent, and corresponded to a maximum absorbed dose of 60 J cm<sup>-3</sup>.

At ALS 11.0.2, we used short dwell time (milliseconds) per pixel per energy for the acquisition of multienergy spectrum maps, controlled by a piezoelectrically actuated beam shutter (Kilcoyne and Tyliczszak 2004). After each image, a 3 s dead-time followed to reset the monochromator and stages, which allowed for a relaxation period, possibly further reducing potential damage. In addition, the thickness of the picokeystone aerogel substrate attenuates some of the incident photon flux before it arrives at the particle in the middle of the picokeystone. For example, at Fe L-edge, 700 eV transmission at the particle was 12–65%, depending on the keystone aerogel thickness and density.

Thus, all of the STXM analyses were performed within the mandated limits: elemental maps were generally acquired at a factor of approximately 1000 below the fluence limit, and XANES stack acquisitions were a factor of approximately 10 below it.

### Analyzing Samples in Aerogel by STXM

#### Mechanical Sample Safety

There is a trade-off between spatial resolution and a safe working sample position. The focused incident X-ray beam is directed through a 70 μm diameter pinhole order sorting aperture (OSA), positioned close to the sample. The distance of the OSA in front of the sample,  $A_0$ , varies with the focal length of a zone plate,  $f$ , such that

$$A_0(\text{max}) = fD_{\text{cs}}/D \quad (5)$$

where  $D_{\text{cs}}$  is the diameter of a central stop blocking undesired X-rays and  $D$  is the outer diameter of the zone plate. The focal length ( $f_E$ ) of a zone plate at a given photon energy ( $E$ ) is given by

$$f_E = D\delta_{\text{rN}}/\lambda_E \quad (6)$$

where  $\delta_{\text{rN}}$  is the width of the Nth outermost zone and  $\lambda_E$  is the photon wavelength. The spatial resolution limit ( $\Delta r$ ) is defined by the zone plate and is given by the Rayleigh criterion

$$\Delta r = 1.22\delta_{\text{rN}} \quad (7)$$

Thus, the shortest  $A_0$  results from acquisition at the highest spatial resolution (smallest  $\delta_{\text{rN}}$ ) at the lowest energy. During ISPE, we used a 25 nm zone plate ( $\delta_{\text{rN}} = 25$  nm,  $D = 240$  μm,  $D_{\text{cs}} = 90$  μm), giving a clearance distance  $A_0 = 500$  μm at the C K-edge (280 eV) and  $A_0 = 2.4$  mm at the Mg K-edge (1300 eV).

The particles, in the middle of picokeystones, were located 200 μm behind the front silicon nitride membranes, which was included in the  $A_0$  distance. Each entire sample assembly was attached with screws to a removable, modified STXM mount, ensuring that nothing protruded in front of the keystone sample. Besides sample safety, this mounting procedure provided three advantages: the reproducible orientation made the comparison of STXM and XRF maps easier, the closed containment volume shielded the sample from most of the carbon deposition from STXM analyses, and the enclosure also protected the sample from laboratory contamination.

We avoided large pressure changes, which might have ruptured the fragile silicon nitride membranes.

Due to the soft X-ray absorption of air, STXM typically operates in an approximately 30 kPa He atmosphere, or under vacuum. As we were mostly limited to working above 700 eV due to attenuation by aerogel, air was less problematic and we merely purged most of the air from the STXM chamber using simultaneous slow evacuation and a He purge, maintaining the internal pressure of the chamber close to atmospheric throughout the purge and analysis.

### *Imaging Tracks in Aerogel*

The depth of focus is a parameter defined by the numerical aperture of the zone plate and varies with wavelength. For the 25 nm zone plate typically used, the depth of field was approximately 1.5  $\mu\text{m}$  at 700 eV and approximately 15  $\mu\text{m}$  at 1500 eV. Working at around 10% transmission (800–1200 eV, depending on aerogel density), the contrast was sufficient to directly image the impact track by mapping the variation in aerogel column density. The high-resolution direct imaging capability coupled with the fine depth of focus meant that we could unambiguously identify associated particles in their impact tracks in the aerogel. By directly imaging aerogel and particles, we were also able to monitor for radiation effects caused by STXM or other techniques. This capability was particularly useful during ISPE, because the hard X-ray microprobes could not detect changes in the distribution or chemistry of major elements Mg, Al, or Si in aerogel picokeystones.

### *Measurement of Aerogel Density*

Attenuation of soft X-rays by silica aerogel prevents the analysis of some elements by STXM for some Stardust samples. For example, the attenuation length of X-rays at the Fe L-edge (approximately 700 eV) in  $\text{SiO}_2$  aerogel with typical density of approximately 25  $\text{mg cm}^{-3}$  is 70  $\mu\text{m}$ . Quantification is unreliable below 5% transmission ( $\text{OD} > 2.9$ ). Therefore, we may not detect an element because of its low abundance or because of energy-dependent attenuation by the aerogel background.

Increased density of a given thickness of aerogel in a picokeystone limits the element edges, which are accessible for analysis in aerogel by STXM. Knowing the density of the aerogel for each tile of the SIDC provides information for planning future extractions of picokeystones. We measured the OD of aerogel for each keystone with respect to the double silicon nitride membrane background ( $I_0$ ) by taking an image of the keystone. We calculated the aerogel density from Equation 2, using the  $\text{SiO}_2$  absorption cross section for that image energy (values from CXRO) and the aerogel thickness. These results are reported for each

picokeystone in the summary tables in the Results sections to follow.

## **RESULTS I: DETECTION OF EXTRATERRESTRIAL IMPACTS**

The principal background for identifying interstellar dust particles in the SIDC was secondary ejecta from impacts on the aft solar panels and from impacts on the interior surfaces of the SRC. These background particles resulted in bona fide impact tracks in the aerogel. A second background present in the collector was numerous contaminants from aerogel manufacture, which can resemble possible impact craters normal to the aerogel surface when scanned from above (as it was in Stardust@home; Westphal et al. 2014b).

Thirty-one ISPE samples analyzed by STXM underwent preliminary screening to characterize the backgrounds in the SIDC aerogel and to develop methods for systematic differentiation of primary extraterrestrial impacts. Measurements are summarized in Table 1.

### **Secondary Ejecta from Impacts on the Aft Solar Panels**

Track trajectories were measured by the shape of the track and assigned a zenith and azimuth coordinate relative to the aerogel collector. For a detailed description of this coordinate system, please refer to Frank et al. (2013). Forty-six tracks identified by Stardust@home had trajectories that could be consistent with an origin as secondary ejecta from impacts on the aft solar panels of the spacecraft (Westphal et al. 2014a). This population has an azimuth of  $20^\circ$ – $160^\circ$  or  $200^\circ$ – $340^\circ$ . Frank et al. (2013) extracted four such samples for analysis: I1017,2,1 (Track 1), I1004,2,3 (Track 3 “Spero”), I1007,1,4 (Track 4), and I1006,1,5 (Track 5). The solar panels were covered with a Ce-rich glass and, as Ce is rare in nature (Ce/Fe approximately  $10^{-6}$ ), the presence of major Ce concentration is strong evidence for anthropogenic material.

The first six extractions from the SIDC, including Tracks 1, 3, 4, and 5 described here, were 350  $\mu\text{m}$  thick keystones, similar to those developed for Stardust cometary samples (Westphal et al. 2004) and not picokeystones optimized later for STXM analyses. The thick aerogel limited possible STXM measurements so that Fe L-edge measurements were not possible, but the diagnostic Ce M-edge at approximately 880 eV was accessible in all four samples, see for example Track 1 shown in Fig. 1. In Table 1, in addition to quantification of Ce, we quantified major elements Al and Mg and detected Na and/or Zn in three of the four

Table 1. Summary of scanning transmission X-ray microscopy preliminary analyses of 31 samples in aerogel.

Sample	Aerogel density, $\text{mg cm}^{-3}$	Aerogel thickness, $\mu\text{m}$	Particle size, $\mu\text{m}$	Elements, phases detected	Impactor origin <sup>1</sup>	Techniques, in order <sup>2</sup>
Low-azimuth impact tracks						
I1017,2,1	$17 \pm 3$	400	1.3 $\mu\text{m}$ diam. and fragments	330 fg Ce, 220 fg Mg, 120 fg Al, 15 fg Zn, K, Ti, Fe	SP	<i>a, b, c, b</i>
I1004,2,3	$25 \pm 2$	350	3.2 $\mu\text{m}$ long	110 fg Ce, 220 fg Mg, Al	SP	<i>d, c</i>
I1007,1,4	$15 \pm 1$	350	1.8 $\mu\text{m}$ diam.	75 fg Ce, 25 fg Zn, 50 fg Na, 12 fg Al, 2 fg Mg	SP	<i>b, c, b</i>
I1006,1,5	$24 \pm 2$	350	3 $\mu\text{m}$ diam.	370 fg Al, 170 fg Ce, 160 fg Mg, minor Na	SP	<i>b, d, b, c</i>
“9 o’clock swarm” population of impact tracks						
I1029,1,6	$16 \pm 2$	400	5 shallow impacts	Mg, Na, Al, two 300 nm corundum grains. Ce n.d.	4 Aer, 1 Cosmic	<i>c, b</i>
I1029,4,10	$17 \pm 4$	70	2 impacts	Weak Na and Al; Ce, Mg, and Fe n.d.	Aer	<i>c, b</i>
Crater-like features						
I1032,1,11	$31 \pm 4$	70	9 $\mu\text{m} \times 4 \mu\text{m}$	33 pg Al as oxide	Anth	<i>c, b</i>
I1006,2,18	n/a	70	n.d.	Damaged, aerogel too dense	n.d.	<i>c, b</i>
I1013,2,19	$22 \pm 3$		11 $\times$ 3 $\mu\text{m}$	Surface particle: Si, Al, Mg	Anth	<i>c, b, c, b</i>
I1017,6,20	$41 \pm 7$	70	3 $\mu\text{m}$ diam.	Surface particle: Na, Mg, Al, Si, Fe, Ni, and Zn n.d.	Anth	<i>b, a, b, c, b</i>
I1004,3,21	$38 \pm 4$	150	50 $\mu\text{m}$ filament	Si; Mg and Al n.d.; too dense for Fe	Anth	<i>b, a, b, c, b</i>
I1031,1,23	$15 \pm 4$	70	3.2 $\mu\text{m}$ diam.	Si-rich, Na, Al, possible Ce	Anth	<i>c, b</i>
I1006,3,24	$23 \pm 3$	70	1.5 $\mu\text{m}$ diam.	Si, Al, Fe, Zn, Ni; Mg and Ce n.d.	Anth	<i>c, b</i>
I1075,1,25	$35 \pm 6$	100	No impact	Particles on cut surface of keystone	Anth	<i>e, c</i>
I1093,2,26	$39 \pm 6$	100	No particles	Triangular imprint feature	Unknown	<i>c</i>
I1059,3,31	$21 \pm 3$	120	Polymer film	Al, Mg in flake	Anth	<i>c</i>
I1044,2,32	n/a	70	n.d.	Damaged, aerogel too dense	Anth <sup>e</sup>	<i>e, c</i>
I1044,3,33	$36 \pm 4$	70	n.d.	350 nm chondritic <sup>e</sup> expected	Possible IDP <sup>e</sup>	<i>e, c</i>
“Midnight” impact tracks						
I1004,1,2	$32 \pm 6$	400	2 $\mu\text{m}$ diam.	Al amorphous oxide; (XRF high Cr, Ni, Zn wrt Fe) <sup>a</sup>	SRC lid	<i>c, e, c</i>
I1060,1,28	$22 \pm 9$	60	8 $\mu\text{m}$ diam. film	Al metal & weak Al oxide	Anth, SC (Mylar)	<i>a, b, c</i>
I1059,2,29	$24 \pm 3$	100	1.6 $\mu\text{m}$ diam.	Al metal	SC	<i>a, b, c</i>
I1043,1,30	$27 \pm 2$	100	2.3 $\times$ 1.0 $\mu\text{m}$	Al, Fe, Mg, Si	Cosmic	<i>af, c, d, c, b</i>
I1047,1,34	$48 \pm 12$	85		Fe, Mg, Si, minor Al	Cosmic	<i>c, af, c</i>
I1032,2,35	$35 \pm 14$	85	Bilobate, each 0.8 $\mu\text{m}$ diam.	2.6 pg Al metal & 0.5 pg Al oxide	SRC, metal plus anodized layer	<i>c</i>
I1032,3,36	$23 \pm 5$	85	2.5 $\mu\text{m} \times 1.5 \mu\text{m}$	0.5 pg Al metal and amorphous Al oxide	SC	<i>c</i>
I1092,1,37	$16 \pm 6$	85	1 $\mu\text{m} \times 0.5 \mu\text{m}$	0.15 pg Al in oxide, 0.19 pg C, minor Fe, ~20 fg FMg, Ni, and Ce n.d.	SRC lid	<i>h, a, c</i>
I1092,2,38	n/a	85	n.d.	Aerogel too dense	Unknown	<i>c</i>
I1017,1,39	$24 \pm 3$	85	0.5 $\mu\text{m}$ diam.	0.27 pg Al metal	SC	<i>c</i>
I1003,1,40	$12 \pm 1$	100	No terminal particle	Possible C, Fe	Cosmic	<i>b, c</i>
I1097,1,41	$34 \pm 4$	75	3 $\mu\text{m} \times 1.5 \mu\text{m}$	22 pg Al metal	SC	<i>i</i>
I1048,1,42	$21 \pm 4$	75	1 $\mu\text{m}$ diam.	1 pg Al metal	SC	<i>c</i>

<sup>1</sup>SP = solar panel glass; Aer = melted aerogel from impact; Cosmic = extraterrestrial material; Anth = anthropogenic contaminant; SRC = Stardust Sample Return Capsule; SC = other spacecraft material; n.d. = not detected.

<sup>2</sup>*a* = XRF at ESRF ID13 (Brenker et al. 2014); *b* = FTIR at 1.4.3 (Bechtel et al. 2014); *c* = STXM at ALS 11.0.2 (this work); *d* = XRF at ESRF ID22 (Simionovici et al. 2014); *e* = XRF at APS 2-ID-D (Flynn et al. 2014); *f* = XRD at ESRF ID13 (Gainsforth et al. 2014); *g* = XRD at ESRF ID22 (Gainsforth et al. 2014); *h* = FTIR at NSLS U2A (Bechtel et al. 2014); *i* = STXM at ALS 5.3.2.1 (this work).

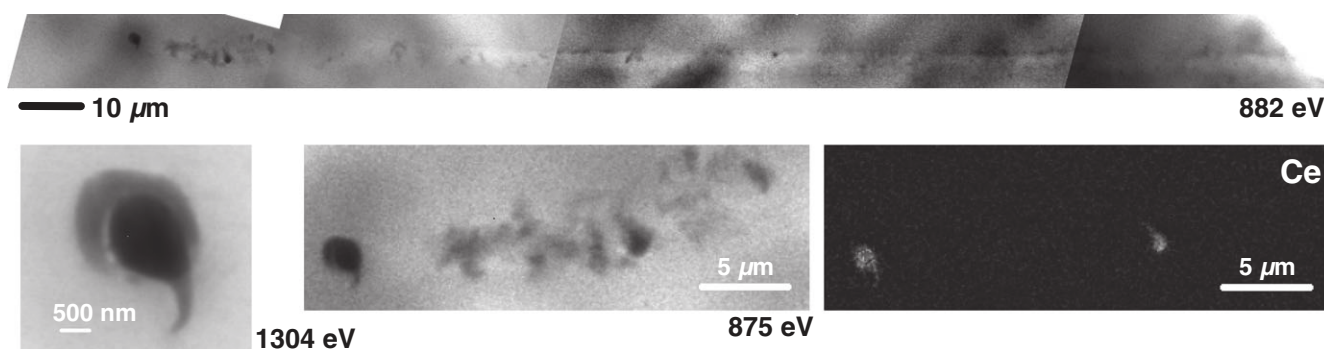


Fig. 1. I1017,2,1. Top, mosaic of 882 eV absorption images of entire track length (268  $\mu\text{m}$  long, 3  $\mu\text{m}$  diameter). Bottom left, image of the 1.3  $\mu\text{m}$  diameter terminal particle image (1304 eV); middle, 875 eV image of 30  $\mu\text{m}$  of track; and, right, cerium map of the same area, showing the terminal particle and one other Ce-rich fragment.

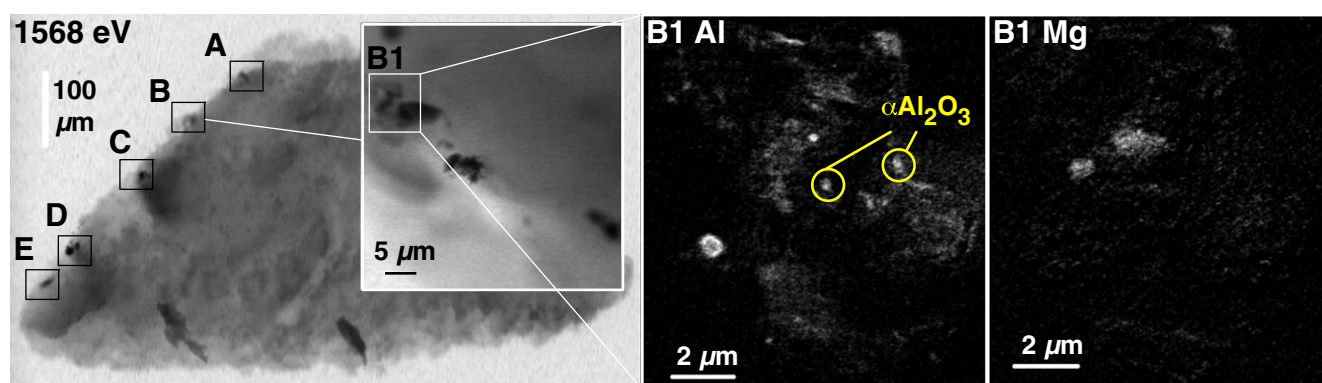


Fig. 2. I1029,1,6 keystone shown in a 1568 eV absorption image. Inset: 1560 eV image detail of region B, which contains several dense subregions. Subregion B1 Mg and Al maps show heterogeneous distributions. Two approximately 300 nm corundum grains were detected among other Al-bearing phases in Al X-ray absorption near-edge structure stack maps (spectrum shown with  $\alpha\text{Al}_2\text{O}_3$  standard in Fig. 3).

tracks. Although compositions varied among the four tracks analyzed, the presence of Ce in all of them strongly suggests that all 46 impacts in the population of angled tracks originate from secondary ejecta from the aft solar panels.

### “9 o’clock Swarm” Population

Tile I1029 contained a large number of apparent impacts originating from the same direction (approximately  $90^\circ$  from interstellar trajectory), which were referred to as the “9 o’clock swarm” (Frank et al. 2013). We rejected the possibility that these impacts were due to interstellar grains because of their abundance, inhomogeneous spatial distribution, and trajectory, but they warranted investigation as possible extraterrestrial impacts (probably originating from within the solar system). Two keystones (I1029,1,6 and I1029,4,10) were extracted and analyzed by STXM, summarized in Table 1.

I1029,1,6 (Track 6) was extracted as a picokeystone, but the thin section detached from the main body of the keystone and was lost. The remaining 400  $\mu\text{m}$  thick keystone contained five impact features from the same impact population in the surface of the aerogel. None of the features contained Ce, thus pointing away from an origin as secondary ejecta from an impact on an aft solar panel. In Fig. 2, we show the features marked A–E. Regions A, C, D, E contained smooth, featureless particles, which were likely to be condensed, melted aerogel.

Al XANES spectra from stack acquisitions of the regions showed differing phases. Most of the particles had one low-intensity single-peak spectrum, consistent with amorphous oxidized Al. In Region B, the Al spectrum was nearly featureless, consistent with amorphous material present as a minor component in all fragments. However, the 10  $\mu\text{m}$  B1 subregion contained a number of small fragments, including Mg- and Al-rich particles. We identified two approximately



300 nm corundum grains from PCA analysis and spectrum fitting of an Al XANES stack and comparison of the spectrum with a corundum standard (shown in Fig. 3). Mg XANES spectra of two other particles (Fig. 2) resembled an augite pyroxene standard, but we did not verify pyroxene composition or address spectral variations due to crystalline orientation. Fe was not detected ( $<2 \text{ fg } \mu\text{m}^{-2}$ ), although the Track 6 aerogel was too thick to be definitive.

The chemical and trajectory evidence suggests that the “9 o’clock swarm” population of impacts may have been the result of an impact and breakup of a solar system object, some of which survived capture in Tile I1029.

### Crater-Like Features

Our initial expectation was that the Interstellar Dust Collection would consist of normal incidence impacts in the aerogel, giving rise to small circular track mouths and circular bulbous, crater-like tracks when scanned from above (Westphal et al. 2014b). Ten of the features identified in Stardust@home most likely to be normal incidence tracks or craters were analyzed by STXM: we looked for micrometer-sized craters or evidence of an impactor  $<500 \text{ nm}$  in diameter. Two additional mysterious features identified by Stardust@home were unlikely to be impacts, but helped to characterize the SIDC aerogel backgrounds. The analyses are summarized in Table 1.

We found no evidence for an impact in samples I1032,1,11, I1013,2,19, I1017,6,20, I1004,3,21, I1031,1,23, I1006,3,24; particles found in each sample are shown in Fig. 4. An Al XANES spectrum from a  $9 \mu\text{m} \times 4 \mu\text{m}$  particle in I1032,1,11 (“T11” in Fig. 3) showed oxidized Al, but not a match for corundum or spinel. These six particles are most likely terrestrial contaminants and not secondary ejecta from the spacecraft.

We conducted coordinated XRF and STXM analyses of two samples (I1075,1,25 and I1044,3,33), which demonstrated the advantage of a multitechnique approach.

#### I1075,1,25 (Track 25)

No impact track was identified when the extracted Track 25 keystone was viewed optically from the side. The keystone was analyzed by XRF (Flynn et al. 2014) and four particles were identified on the original surface and in the main body, together forming a line, which could have formed an impact track. In STXM, we located the region of particles named “A and B” by Flynn et al. on the top cut surface of the aerogel keystone. We imaged the aerogel at different focal

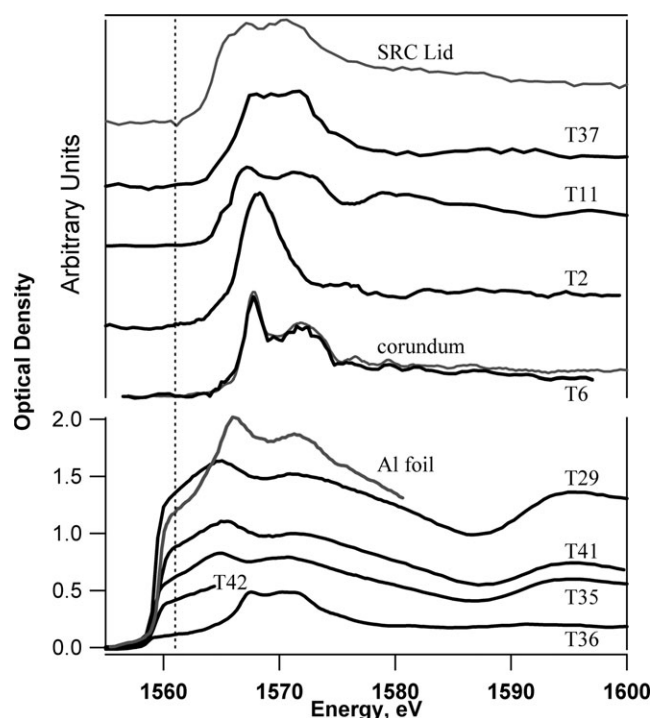


Fig. 3. Al X-ray absorption near-edge structure spectra of Stardust Interstellar Dust Collector backgrounds. Upper plot: spectra from I1092,1,37 (T37) and I1032,1,11 (T11) are similar to a spectrum of amorphous oxidized Al from the anodized SRC lid (Frank et al. 2013); I1004,1,2 (T2) is amorphous oxidized Al. I1029,1,6 (T6) originating from unknown solar system material, fits to corundum (gray). The maxima ranged from OD 0.2 to 1.1; the spectra were normalized at 1590 eV. Lower plot: spectra from an Al foil standard (gray) and five impact tracks containing Al metal (I1059,2,29 “T29,” I1032,2,35 “T35,” I1032,3,36 “T36,” I1097,1,41 “T41,” I1048,1,42 “T42”). Track 36 also contains oxidized Al similar to Track 37 and the SRC lid. The vertical axis values are  $\Delta\text{OD}$  (Equation 3), which relate to the mass of Al metal (Equation 5). The dashed line shows the energy used for mapping of Al metal, 1561 eV, and illustrates the clear difference between Al metal and oxidized Al spectra.

depths through the picokeystone and found no evidence of an impact track (878 eV and 1313 eV energies provided high contrast images of the aerogel). We concluded that the particles detected by XRF were probably contamination and that their spatial distribution was coincidental, and that the original feature found in Stardust@home was probably an inclusion in the aerogel formed during manufacture.

#### I1044,3,33 (Track 33)

We initially searched the area in Track 33 suggested from optical microscopy, between 40 and 90  $\mu\text{m}$  from the corner of the picokeystone, and found no particles (Fig. 5). Subsequent XRF analysis at APS 2-ID-D detected approximately 10 fg Fe in an approximately

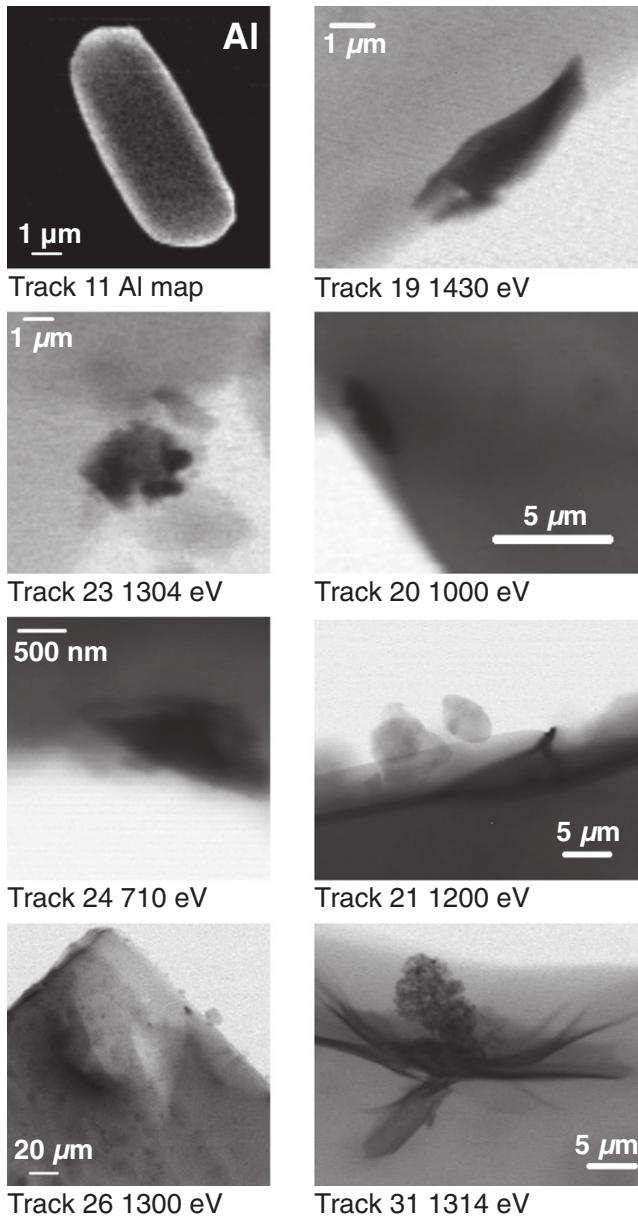


Fig. 4. Crater-like features identified in Stardust@home. Al map from I1032,1,11 (Track 11) and X-ray absorption images of I1013,2,19 (Track 19 1430 eV image), I1017,6,20 (Track 20 1000 eV image), I1004,3,21 (Track 21 1200 eV image), I1031,1,23 (Track 23 1304 eV image), I1006,3,24 (Track 24 710 eV image), I1093,2,26 (Track 26 1300 eV image of indent feature viewed from the side), I1059,3,31 (Track 31 1314 eV image)

200 nm particle, which might have a heavy element profile consistent with an extraterrestrial projectile (Flynn et al. 2014). That feature was situated 30  $\mu\text{m}$  from the picokeystone corner. XRF imaging has a very large depth of field, however, and it remained a possibility that the Fe hotspot detected at 2-ID-D was

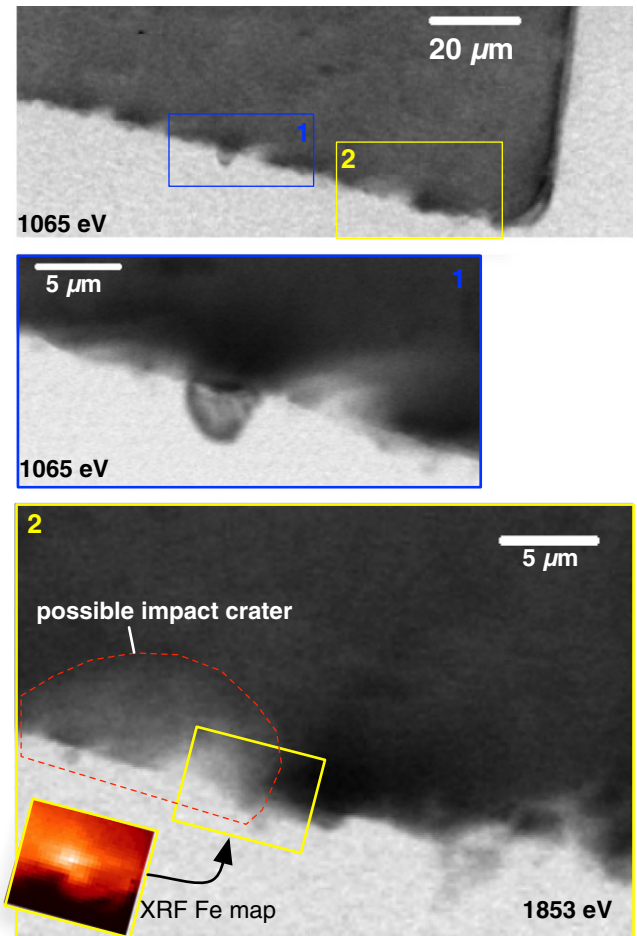


Fig. 5. X-ray absorption images, at the energies shown, of search regions labeled 1 and 2 in I1044,3,33 (Track 33). We did not find the 200 nm Fe-bearing particle, discovered by Flynn et al. (2014), shown in the scaled X-ray fluorescence (Fe  $K\alpha$ ) map. We identified a possible crater feature in the aerogel.

on one of the cut aerogel surfaces. We searched again at 5  $\mu\text{m}$  depth intervals through the aerogel keystone in the matched region and found no particles or evidence of Fe, Mg, or Al. It is possible that the effective detection limit was  $>10 \text{ fg Fe}$  for STXM measurements on Track 33 because of a combination of three factors: (1) The high OD aerogel in Track 33 increased background noise, thus raising the postedge Fe detection limit to  $5 \text{ fg } \mu\text{m}^{-2}$ , (2) the unknown depth of the Fe particle was missed by the 1.5  $\mu\text{m}$  focal depth of the 700 eV STXM images, (3) the unknown Fe phase had low resonance enhancement. It is therefore possible we could have missed a 200 nm Fe particle at unknown depth in the aerogel. Further XRF measurement made at a different angle could confirm the presence of Fe and estimate its three-dimensional position, after which STXM reanalysis could be attempted.

We imaged a crater-like feature (Fig. 5, Region 2), which had a morphology consistent with formation by a high-speed projectile incident on the aerogel surface at a significant zenith angle. Based on the orientation of the picokeystone with respect to the SIDC tray, we determined that the most likely azimuth angle of the impactor would have been approximately  $90^\circ$  from the expected arrival direction of most interstellar dust (Sterken et al. 2014). However, a small fraction of interstellar dust is expected to arrive from this direction. To add further uncertainty, crater morphologies from complex, irregular projectiles can deviate significantly from symmetrical shapes, even at normal incidence (Wozniakiewicz et al. 2009).

I1093,2,26: Stardust@home searches discovered a number of paired triangular features in the surface of tile I1093. One example of these features was extracted in a  $100\text{ }\mu\text{m}$  thick picokeystone. We noted denser aerogel beneath the imprint feature, shown in “Track 26” (Fig. 4). We did not detect any particles or find evidence for the cause of these triangular features.

I1059,3,31: Stardust@home flagged a possible “spider-like” impact feature, about  $23\text{ }\mu\text{m}$  in diameter, which was extracted in a  $120\text{ }\mu\text{m}$  thick picokeystone. STXM analysis showed metallic and oxidized Al and Mg in the surface feature, which had the morphology of a flake or foil. The origin was probably surface contamination from an aluminized thin polymer.

I1006,2,18 was successfully extracted, but the picokeystone was partially crushed during sample handling, resulting in greater column density of aerogel at the region of interest. We mapped for Mg, but detected none, and the keystone was too thick for Fe measurement.

I1044,2,32 was also successfully extracted, but the keystone shriveled and became too dense for any STXM analyses, possibly from outgassing from cyanoacrylate used in mounting the silicon nitride frames.

### Midnight Tracks: Trajectories Originating from Secondary Impacts on the Sample Return Capsule or from the Interstellar Dust Stream

The Stardust collector was tilted during the SIDC exposures so that the normal vector to the surface of the tray pointed toward the predicted radiant direction for interstellar dust with  $\beta = 1$  ( $\beta$  is solar wind force/gravitational force). Because of this orientation, secondaries that might have originated from impacts on the SRC have trajectories that are identical to those originating from the interstellar dust stream. Both populations belong to the so-called “midnight” track

population with azimuth less than  $\pm 21^\circ$  (Frank et al. 2013). Twenty five tracks were discovered belonging to this population, including 23 found in Stardust@home and two detected in the laboratory. Because there were no impact detectors on the collector that could give information on impact timing, there is an inherent ambiguity regarding the origin of the midnight track particles. Thirteen midnight tracks were extracted and their preliminary characterizations by STXM are summarized in Table 1.

The Stardust SRC comprised Al metal with an anodized coating. Fortunately, Al metal is straightforward to recognize in Al XANES spectra, because of the 6 eV spectral shift of the metal Al edge toward lower energy compared with all oxidized Al species, and Al does not exist in the metallic state in nature. Spectra from acquired Al XANES stacks in five samples (I1059,2,29, I1032,2,35, I1032,3,36, I1097,1,41, I1048,1,42) exhibited the 1559 eV Al metal edge, shown in Fig. 3 with an Al foil for comparison. We measured the density of Al in I1059,2,29 to be approximately  $2.8\text{ g cm}^{-3}$ , in agreement with the  $2.7\text{ g cm}^{-3}$  value for metallic aluminum. We also found that the  $\Delta\text{OD}$  measured between 1561 eV and 1555 eV provided a reliable estimate of Al metal mass (using Equation 3). In I1017,1,39, we simply acquired a two-energy map to characterize the  $0.26\text{ }\mu\text{m}^2$  terminal particle as 0.27 pg Al metal spacecraft. Images and Al maps of these six SRC metal background samples are shown in Fig. 6.

In addition to its minor Al metal component, the I1032,3,36 spectrum (“T36” in Fig. 3) also showed a stronger peak at 1568 eV, corresponding to oxidized Al. This material was broadly consistent with the anodized layer in the SRC lid, shown also in Fig. 3. See Frank et al. (2013) for details of the SRC sampling.

### I1060,1,28 (Track 28)

The I1060,1,28 terminal particle (Fig. 6a) was verified as being associated with an impact track, but its morphology resembled the film captured on the surface of I1059,3,31. The particle appeared to be different from previously acquired XRF maps (Brenker et al. 2014), which could be due to the carbon film not being imaged by XRF, or due to hard X-ray modification. Subsequent optical images of the terminal particle bear close resemblance to the STXM X-ray absorption images. From Al chemical mapping (1561 eV corresponds to Al metal, 1568 eV to oxidized Al), we found  $2\text{ }\mu\text{m}^2$  Al metal surrounded by weak oxidized Al conforming to the particle’s low-Z density distribution. The heavy element profile (Brenker et al. 2014) notably did not match Al metal from the SRC deck; the origin of Track 28 could be a secondary impact on Mylar film



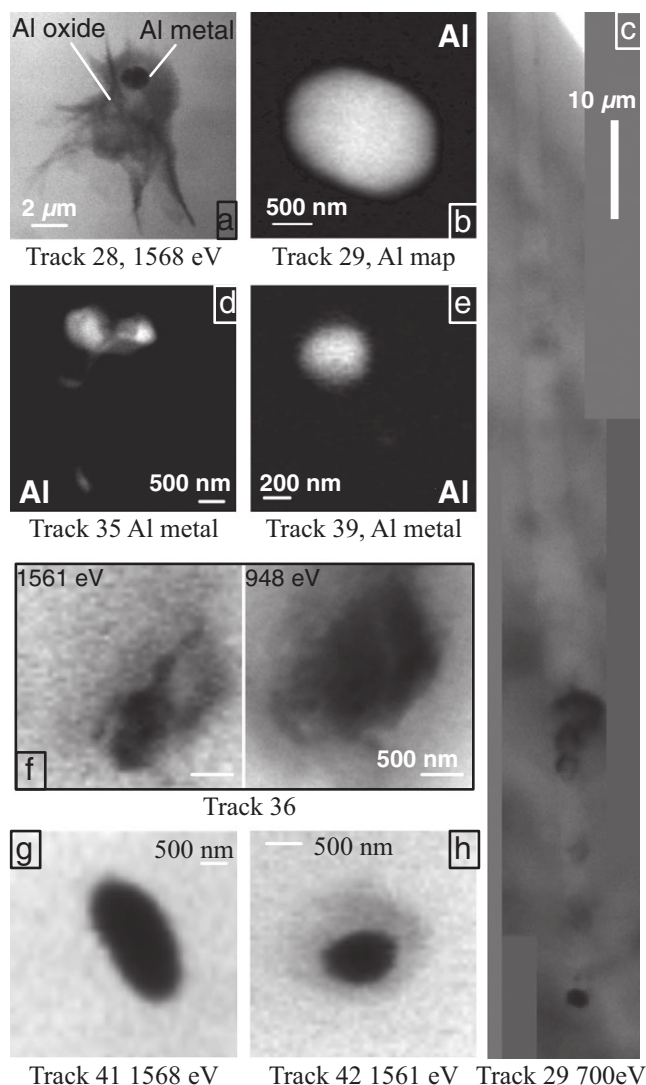


Fig. 6. Midnight tracks with origins from secondary impacts on the Stardust SRC deck. a) Absorption image of I1060,1,28 Mylar foil, b) I1059,2,29 Al metal map and c) absorption image of aerogel track; metallic Al maps of d) I1032,2,35 and e) I1017,1,39; absorption images of f) I1032,3,36 Al and low-Z components and Al metal particles in g) I1097,1,41 and h) I1048,1,42.

present around the SRC deck. No sample of the SRC Mylar was available for comparison.

#### I1092,1,37 (Track 37, Merlin)

We mapped oxygen and silicon occurring as a melted aerogel shell around the particle and we detected minor Fe in the  $0.45 \mu\text{m}^2$  terminal particle “Merlin.” The low aerogel density ( $16.3 \pm 6 \text{ mg cm}^{-3}$  measurement from a 1000 eV image) allowed us to make a limited C measurement. We estimated 0.19 pg of C from a 310 eV map (the aerogel was optically dense in the 280 to 300 eV C XANES energy range).

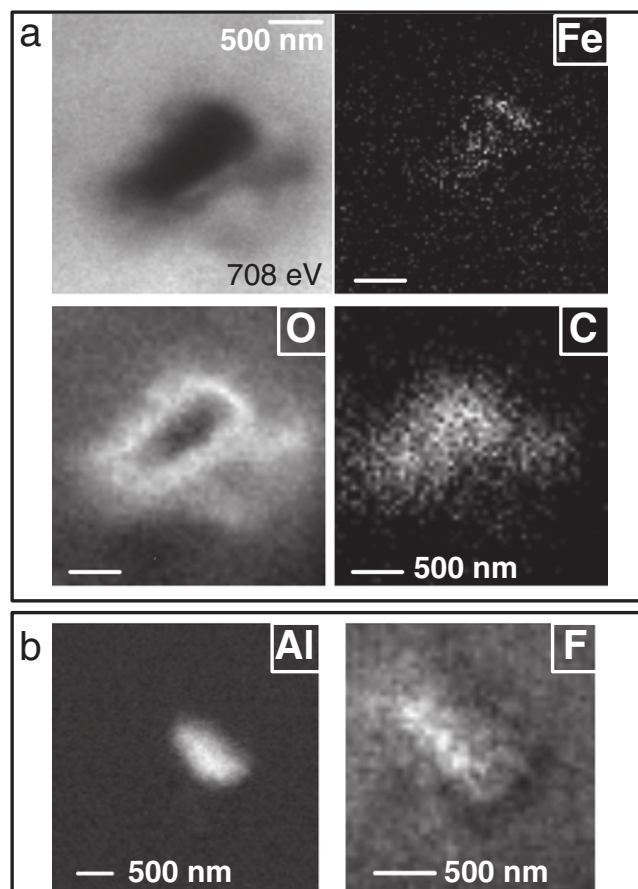


Fig. 7. Characterization of I1092,1,37. a) Absorption images of the terminal particle “Merlin” and Fe, C, O maps. b) In a different orientation, Al and F maps. F signal is weak, but signifies a match with SRC lid anodized material.

We characterized a sample of a carbon-rich region of the SRC lid anodized surface by SEM (Frank et al. 2013) and found that it also contained cosmically rare F; and we subsequently detected approximately 20 fg F in Merlin (the F K-edge at 697 eV lies on the tail of the O K-edge peak, giving a rather weak signal against a large  $\text{SiO}_2$  background).

The spectrum from an Al XANES stack (“T37,” Fig. 3) showed no Al metal, but 0.15 pg Al oxide (not corundum) was present in the particle core. The  $\text{Al}_2\text{O}_3$  density was approximately  $1.3 \text{ g cm}^{-3}$ . The spectrum was not an exact match for the amorphous Al oxide in the sample of SRC lid anodized coating (also shown in Fig. 3), which could be due to SRC heterogeneity or capture effects in aerogel.

Merlin was unlike the other background spacecraft secondary impacts, considering the lack of Al metal and an excess of carbon. We found a probable match with the Stardust anodized SRC lid material. Figure 7 shows the C, O, Fe, Al, and F elemental maps for this particle.



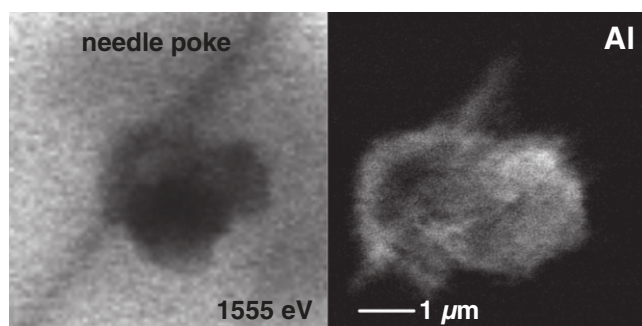


Fig. 8. I1004,1,2 1555 eV X-ray absorption image and an Al map showing the terminal particle and a needle-poke from the extraction process.

### *I1004,1,2 (Track 2)*

The high-density aerogel background ( $32 \pm 6 \text{ mg cm}^{-3}$ ) made it difficult to image this track directly, but we did see a needle-poke extending through the particle, consistent with an unintentional move during the keystone extraction procedure (Fig. 8). Al XANES analysis indicated a simple amorphous aluminum oxide spectrum (“T2,” Fig. 3), with some Al smearing into the needle poke. Coordinated XRF analysis of the same track (Flynn et al. 2014) also showed Fe smearing into the needle-poke—confirmation that we analyzed the same particle. The density was too high to measure Ce, Ni, or Fe; an Mg measurement was possible, but we detected none.

The trajectory of Track 2 is consistent with an origin either as interstellar dust or as a secondary from the SRC deck: STXM results could not discriminate between these possibilities and Flynn et al. (2014) concluded that an extraterrestrial origin was unlikely based on the particle heavy element abundances.

I1092,2,38 (Track 38): Some distortion occurred during transfer of Track 38 to the silicon nitride window sandwich, which condensed the aerogel keystone. Although optically the track appeared unaffected, the resulting aerogel around the track was too dense for any STXM analysis, and its origin remains ambiguous.

We performed preliminary screening analyses on I1043,1,30, I1047,1,34, and I1003,1,40 in the same way as for the other midnight tracks described in this section, Table 1. Navigation images confirmed impact tracks in all three samples and Al XANES ruled out the presence of Al metal in Tracks 30 and 34.

Following the initial characterization of spacecraft and contamination materials, we were able to reject a large number of samples from further consideration (even those with a plausible interstellar trajectory) and focus on the three midnight tracks remaining as interstellar candidates, which are described in detail in the next section.

## RESULTS AND DISCUSSION II: ANALYSES OF THREE TRACKS OF PROBABLE EXTRATERRESTRIAL ORIGIN

### *I1043,1,30 (Track 30, Orion/Sirius)*

I1043,1,30 was discovered through Stardust@home (Westphal et al. 2014b). The first “duster” to identify Track 30 was Bruce Hudson, who named the sample Orion; the feature was promoted to the Stardust@home Red Team’s short list by Fred Grey. The extracted track was 75  $\mu\text{m}$  long in a 100  $\mu\text{m}$  thick picokeystone; see Frank et al. (2013). Track 30 was first analyzed by XRF/XRD at ESRF beamline ID13, where the sample was oriented  $45^\circ$  to the X-ray beam, and Brenker et al. (2014) reported finding one Fe-rich terminal particle. Subsequent analyses were all oriented with the track normal to the beam. STXM analyses, grouped as “STXM1,” were followed by XRF/XRD at ESRF beamline ID22 (Simionovici et al. 2014), then further STXM analyses are grouped as “STXM2.” These STXM measurements are summarized in Table 2.

#### *STXM1: Post-ID13, Pre-ID22 Analyses of I1043,1,30*

The first STXM X-ray absorption images of Track 30, taken after the XRF/XRD analyses at ESRF ID13, are shown in Fig. 9. We unexpectedly detected a dark crack midtrack and a second particle approximately 3  $\mu\text{m}$  upstream of Orion, which Bruce Hudson later named Sirius. We noted a  $45^\circ$  angled line in the aerogel focused directly on Orion, extending beyond the track, which we associated with the beam footprint in the aerogel left by ESRF ID13—confirmation that both groups analyzed the same particle. We determined that the track diameter was 1.5  $\mu\text{m}$  and the aerogel density was  $26.7 \pm 2 \text{ mg cm}^{-3}$ .

We mapped the whole track (coarse 100 nm to 250 nm pixels) and detected Al, Mg, and minor Fe in the Orion particle; Mg, weak Fe, but no Al (<20 fg) in Sirius; and Fe, <50 fg of Al, but no Mg in the midtrack crack. Because we limited the photon dose acquiring these maps, the weak Fe signal was only slightly above noise ( $\pm 5 \text{ fg } \mu\text{m}^{-2}$  Fe). We did not attempt to quantify Fe during STXM1, but we remeasured Track 30 Fe during STXM2 (below).

#### *STXM1 Characterization of Orion*

Fine (15 nm pixel) Mg, Al, and Fe maps of Orion (Fig. 10) showed that the major elements Al and Mg are closely correlated in the 2.3  $\mu\text{m}$  by 1.0  $\mu\text{m}$  particle. Weak Fe was distributed over Orion, but the brightest spot does not correlate with the brighter Mg regions.

From an Al XANES stack (50 nm pixel images), we quantified  $425 \pm 25 \text{ fg}$  total Al. Spectral fitting showed

Table 2. STXM analyses of I1043,1,30 grouped in chronological order.

Sample region	Measurement <sup>b</sup>	Pixel size ( <i>X</i> , <i>Y</i> )	Dwell per pixel	Quantification	Result, reference <sup>c</sup>
Orion <sup>a</sup>	XRF/XRD at ESRF ID13			800 ± 100 fg Fe	<i>ISPE5</i>
<i>STXM1</i>					
Track, Orion, Sirius	Al map	250 nm	1 ms		Al in Orion, not Sirius
Midtrack and crack	Al map	50 nm	1 ms	<50 fg Al in track	
Whole track	Fe maps	200 nm	4 ms	n.d.	Weak Fe signal
Midtrack and crack	Fe map	100 nm	4 ms	n.d.	Weak Fe signal
Track, Sirius	Mg map	100 nm	1 ms	Mg in Sirius	Mg not detected in track
Orion	Al map	15 nm	2 ms		
Orion	Fe map	15 nm	2 ms		
Orion	Mg map	15 nm	2 ms		
Orion	Al stack	75 nm	1 ms	425 ± 25 fg Al	
Sirius	Fe map	15 nm	2 ms	2 ± 10 fg Fe	Low signal: noise
Sirius	Mg map	15 nm	2 ms		
Sirius	Mg stack	70 nm	1 ms	300 ± 60 fg Mg	
Orion, partial Sirius	<i>XRF/XRD at ESRF ID22</i>			Orion 38 ± 2 fg Fe	<i>ISPE7</i>
<i>STXM2</i>					
Whole track and crack	Fe map	133 nm	6 ms	550–2200 fg Fe	
Whole track and crack	Ni map	133 nm	5 ms	n.d.	
Midtrack and crack	Si map	50 nm	20 ms		
30 μm track, Orion, Sirius	Mg map	50 nm	2 ms		
10 μm track, Orion, Sirius	Fe map	25 nm	2 ms	30 ± 10 fg Fe	
10 μm track, Orion, Sirius	Ni map	50 nm	10 ms		
Orion	Mg stack	50 nm	1 ms	200 ± 40 fg Mg	
Orion	Fe stack	33 nm	2 ms	12–20 fg Fe	
Orion	Si stack	20 nm	2.4 ms	200 ± 200 fg Si	
A) Sirius fragment, B) Orion	Mg stack	50 nm	1 ms		
Sirius fragment	Fe stack	33 nm	2 ms	<3 fg Fe	
Sirius fragment	Si stack	50 nm	1 ms		

STXM = scanning transmission X-ray microscopy; XRF = X-ray fluorescence; XRD = X-ray diffraction; ESRF = European Synchrotron Radiation Facility; ISPE = Interstellar Preliminary Examination.

<sup>a</sup>Single terminal particle analyzed at ID13.

<sup>b</sup>An element map is a 2-image acquisition at energies above and below the absorption edge; A stack is a multi-image acquisition performed at stepped energies, from which XANES spectra and maps may be derived.

<sup>c</sup>ISPE5: Brenker et al. (2014) and ISPE7: Simionovici et al. (2014).

that the same spectrum was present throughout Orion, shown in Fig. 11 along with various Al standards analyzed on the same beamline. The oxidized Al standards and Orion do not have significant absorption at 1561 eV, thus differentiating them from spacecraft Al metal. To further rule out spacecraft ejecta, we compared the Al XANES of Orion with oxidized Al in the anodized section of the Stardust SRC deck (“SRC Lid” in Fig. 11), which was prepared using the FIB lift-out technique (Frank et al. 2013). The Orion Al spectrum had a significant first EXAFS peak at 1588 eV, showing a type of order different from the amorphous anodized SRC lid, which does not show the EXAFS peak. Orion also contained significant Mg (quantified during STXM2), but we found that the SRC lid Mg content was <1%.

Orion appeared to show a mixed coordination environment for Al. The Al spectrum is a reasonable

match for a spinel-like structure (coordination number, CN = 6), but shifted approximately 2 eV toward lower energy compared with the spinel standard (MgAl<sub>2</sub>O<sub>4</sub>). The first spinel peak is 1567 eV (Neuvill et al. 2009); the first corundum peak (also CN = 6) is at 1568 ± 0.6 eV (Li et al. 1995; Ildefonse et al. 1998; Mottana et al. 1998; Neuvill et al. 2009).

The lower 1565 eV peak corresponds to four-fold symmetry and could be due to transfer to CN = 4 in high-temperature inverted spinel or Al-rich spinel (Neuvill et al. 2009); or it could be due to an admixture of CN = 4 aluminosilicate, for example, we show oligoclase (80% albite, 20% anorthite) in Fig. 11. Gainsforth et al. (2014) report diffraction evidence in Orion for well-distributed spinel crystallites, a single olivine grain, and an unknown phase. This implied that the larger fraction of the Al-bearing phase was amorphous, which was consistent with the

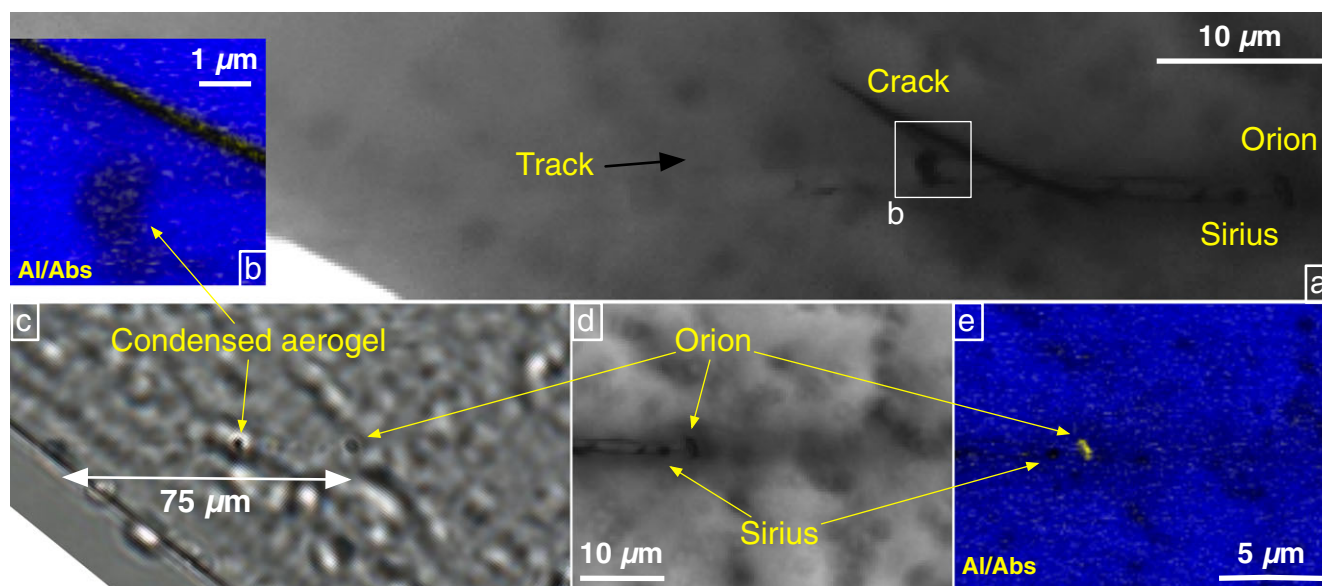


Fig. 9. I1043,1,30 (Track 30) X-ray absorption images and Al maps taken during experiment ‘STXM1’ (see text). a) 708 eV absorption image shows the whole track, a dark crack, and two particles, Orion and Sirius; b) Al map (yellow) and 1555 eV absorption image (blue) of part of the dark crack and a condensed aerogel particle; c) optical micrograph taken before any analyses (Frank et al. 2013), in which Orion is visible, but not Sirius; d) 704 eV absorption image shows darkened aerogel footprint from ID13 beam extending beyond the track e) Al map (yellow) and 1555 eV absorption image (blue) shows that Al is concentrated only in Orion. (see online version for color figure.)

homogeneous distribution of a broad Al XANES spectrum throughout Orion. Brenker et al. (2014) detected minor Ca, Cr, and Mn by XRF, which could be associated with the Al-rich phase. We also found Mg correlated with Al, which we investigated during STXM2.

#### STXM1 Characterization of Sirius

A Mg map (15 nm pixel) showed near-homogeneous distribution over the 1.5 μm diameter Sirius particle (Fig. 12), its center situated 3 μm from Orion’s center. We derived an abundance of  $300 \pm 60$  fg of Mg from an 85 nm pixel Mg XANES stack of Sirius; the Mg spectrum was homogeneously distributed over the particle. The Sirius Mg spectrum did not match any of the Mg standards analyzed at ALS 11.0.2 (see Fig. 16), ruling out crystalline spinel, periclase, and enstatite; olivine remained a plausible, but poor, fit. Further interpretation of the Track 30 Mg XANES spectra follows the STXM2 analyses (below).

We acquired one high spatial resolution Fe map (15 nm pixels). Although transmission was optimal (OD approximately 1), the Fe signal was weak and the images were affected by episodic beamline noise. We did not attempt an Fe stack at this time, but estimated that Sirius contained  $<10$  fg Fe. From Al maps of the track (Fig. 9), we determined that Al was below detection

limit in Sirius. A Si stack (100 nm pixel) suggested  $200 \pm 50$  fg Si above background aerogel, but the acquisition was affected by beamline noise.

#### STXM2: Post-ID22 Analyses of I1043,1,30

Following the STXM1 run, Track 30 was analyzed by XRF/XRD on ESRF beamline ID22 (Simionovici et al. 2014) and both Orion and Sirius were detected. During these analyses, the sample was inadvertently subjected to a fluence of hard X-rays that exceeded the fluence limits set for ISPE by about an order of magnitude, and the dispersal of heavy elements from Sirius was observed. Subsequent STXM analyses are grouped as “STXM2” in Table 2.

We remapped Mg, Fe, and Ni in the track and compared the distribution in STXM2 with Mg in STXM1 (Fig. 13). We identified Orion, and observed that it retained approximately the same morphology as observed in STXM1, but in place of Sirius, we observed numerous submicrometer-sized, Mg-rich particles.

The STXM2 Fe map had a longer dwell time per pixel than during STXM1, to improve the signal:noise, but we limited ourselves to a two-energy map to minimize fluence, which reduced quantification accuracy. The result showed total mass in the range 550–2200 fg Fe dispersed around the track and crack feature; ID13 XRF had detected  $840 \pm 100$  fg Fe only



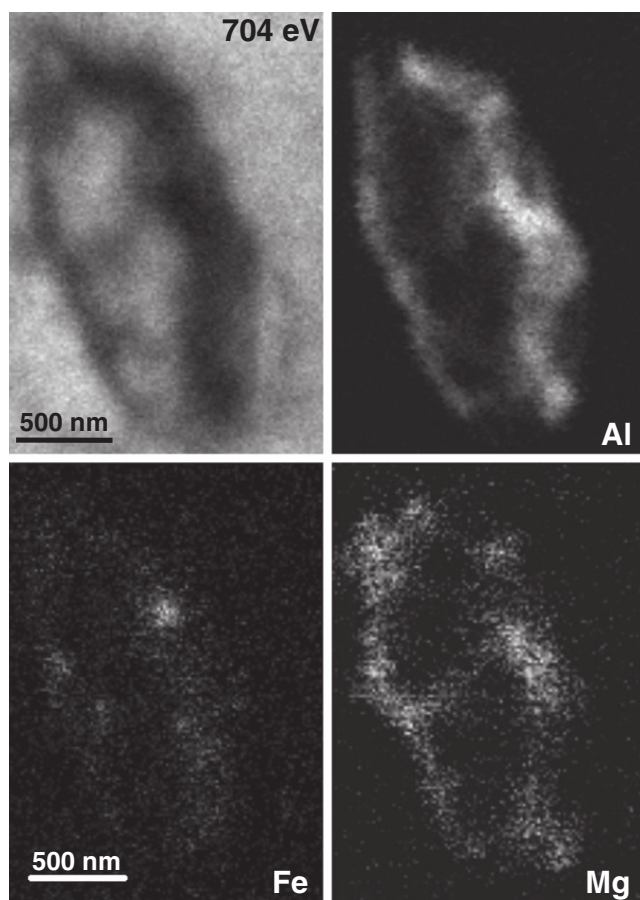


Fig. 10. 15 nm step maps of Orion taken during scanning transmission X-ray microscopy 1, aligned and at the same scale. Clockwise, 708 eV image, Al map, Mg map, and Fe map.

present in Orion. We detected weak Ni present in the midtrack crack with low signal-to-noise ratio.

We mapped the 10  $\mu\text{m}$  length of the end of the track containing Orion and the dispersed Sirius fragments in Fe and Ni at higher resolution (25 nm and 50 nm pixels, respectively). These are shown in Fig. 14 with a subregion of the 50 nm pixel STXM2 Mg map (Fig. 13) for comparison. Fe totaled approximately 30 fg (approximately  $\pm 10$  fg) for this track-end region. Fe was not well correlated with Ni or Mg in the region of the dispersed Sirius fragments.

We also show an XRD topograph from the ID22 analyses in Fig. 14 (Gainsforth et al. 2014). The ID22 scan partially covered the area of Sirius fragments, including Orion (the area labeled B), but excluded the largest Sirius fragment (the area labeled A), where we acquired Fe- $L_3$  and Mg K-edge XANES stacks. The topograph is the sum of all diffraction peaks detected in each coordinate, which showed that Orion contained crystalline material, but the Sirius fragments were amorphous.

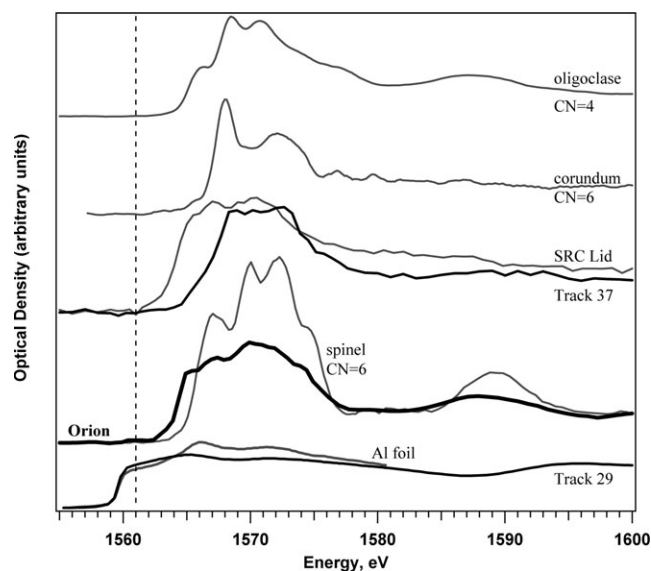


Fig. 11. Comparison of Orion Al X-ray absorption near-edge structure spectrum with standards (in gray). Oligoclase ( $\text{Na, Ca}[\text{Al}(\text{Si,Al})\text{Si}_2\text{O}_8]$ ) has Al in coordination number, CN = 4; spinel and corundum ( $\alpha\text{-Al}_2\text{O}_3$ ) both have Al in CN = 6. Also shown are: spectra from a sample from the SRC Lid (anodized Al) and Track 37 (black line), which is thought to originate from the SRC Lid; and spectra from Al metal foil and Track 29 (black line), which comprises Al metal thought to originate from the spacecraft. The dashed line marks the energy, 1561 eV, corresponding to the edge jump magnitude for Al metal, and no absorption occurs in any other Al X-ray absorption near-edge structure spectrum at energies below this line. Orion maximum OD was 0.35 above background aerogel OD approximately 0.25; all spectra were normalized.

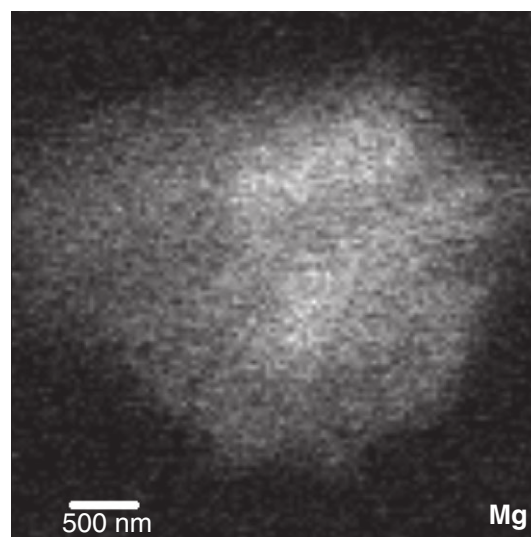


Fig. 12. 15 nm pixel Mg map of Sirius acquired during experiment 'STXM1' (see text).

#### STXM2 Characterization of Orion

We used the Cluster Analysis module of aXis2000 (Jacobsen et al. 2000 and Lerotic et al. 2005), based on



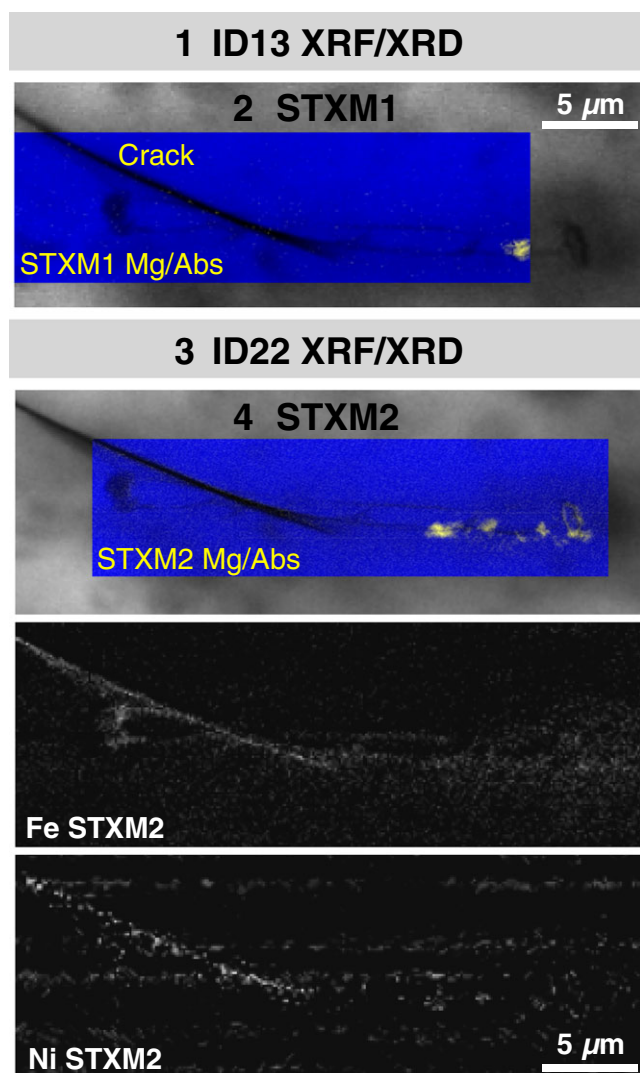


Fig. 13. Comparison of Track 30 during experiments STXM1 and STXM2. 1) ID13 hard X-ray analyses. 2) STXM1: 708 eV absorption image of Track 30 with overlaid STXM1 Mg map (yellow) and 1300 eV absorption images (blue). 3) ID22 hard X-ray analyses. 4) STXM2 maps, scaled and aligned with STXM1: 705 eV absorption image overlaid with STXM2 Mg map (yellow) and 1300 eV absorption image (blue); Fe long dwell time (6 ms pixel<sup>-1</sup>) map; Ni map (5 ms pixel<sup>-1</sup>) shows Ni in the diagonal crack, at approximately twice the level of horizontal noise bands. (see online version for color figure.)

Principal Component Analysis, to analyze the STXM2 Mg XANES stack of Orion. We found a two-component fit to the spectrum at each pixel and mapped the distribution of the two distinct component spectra (Fig. 15). One spectrum constituted 95% of the total Mg, and was distributed over Orion. From the component sum spectrum, we calculated a total of  $200 \pm 40$  fg Mg in Orion. The second spectrum, representing the remaining 5% of the post-ID22 Orion Mg mass, was qualitatively similar to that of Sirius

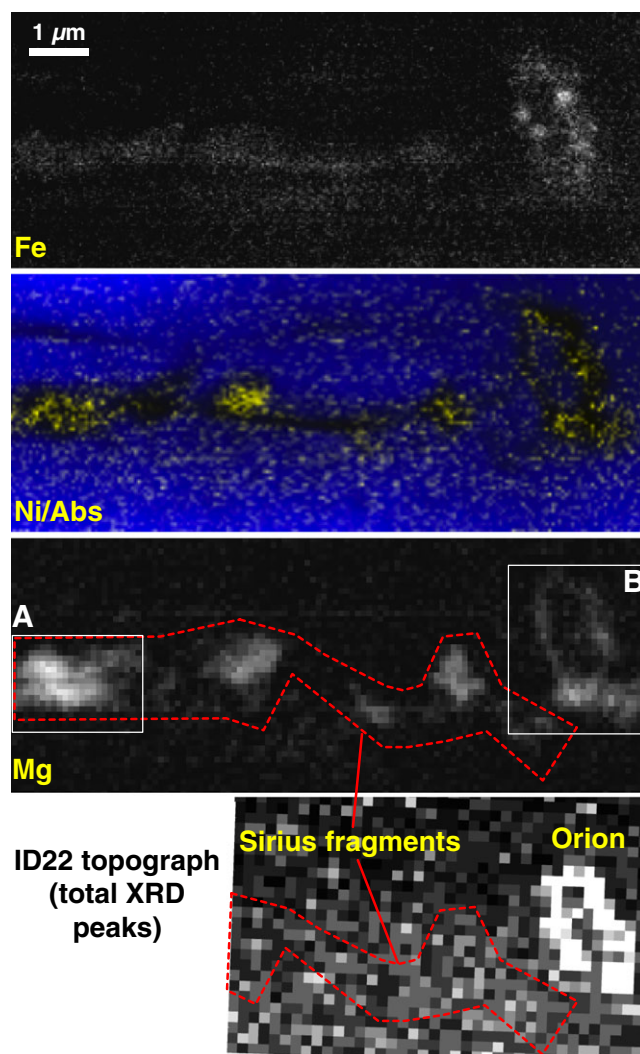


Fig. 14. High-resolution maps of Orion and Sirius during STXM2, summarized in Table 2. From the top: Fe map; Ni map (yellow) and 849 eV absorption image (blue); a subregion of the Mg STXM2 map (Fig. 13), showing the areas of the STXM2 Mg X-ray absorption near-edge structure stack, A and B, and the fragments of Sirius (red outline); X-ray diffraction total peak topograph from ESRF ID22 (Gainsforth et al. 2014) showing crystalline material present in Orion, while Sirius fragments are amorphous. The topograph was scaled and aligned using the ID22 synchronous X-ray fluorescence map (Simionovici et al. 2014). (see online version for color figure.)

during STXM1 and of the largest Sirius fragment (below). We had, therefore, means of separating Mg native to Orion from the contaminating fragments of Sirius.

The Orion component spectrum is most consistent with Mg-spinel  $\text{MgAl}_2\text{O}_4$  and is a poor match to other standards (e.g., periclase, olivine, or enstatite). The peak energies (the A-B-C triplet) match well to those of spinel, but the relative intensities are lower than the

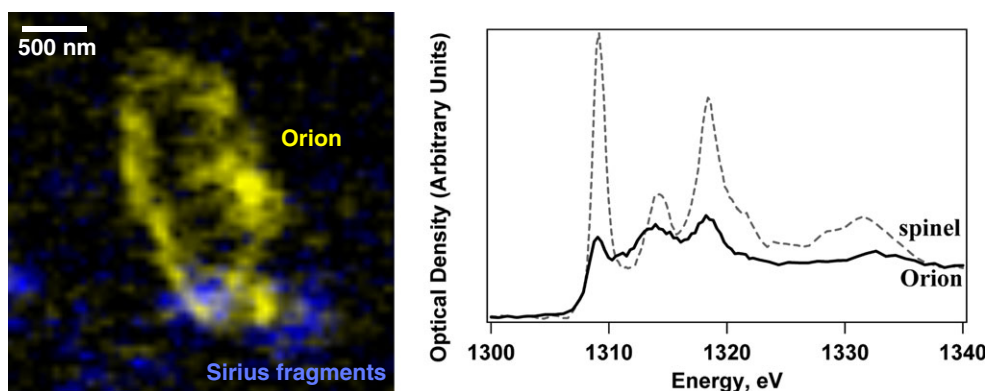


Fig. 15. Principal Component Analysis of STXM2 Mg X-ray absorption near-edge structure stack spectra, from Fig. 14 Region B, revealed two-component spectra mapping to Orion (yellow) and the Sirius fragments (blue), shown left. The Orion spectrum A-B-C and D peaks match well to  $\text{MgAl}_2\text{O}_4$  spinel (spectrum maximum OD 0.4 above aerogel OD 0.4, normalized with a spinel standard spectrum at 1340 eV). The lower intensity peaks were consistent with more disordered material. The Sirius Mg spectrum comparison is shown in Fig. 16. (see online version for color figure.)

crystalline standard. Together, the Mg spectrum (STXM2), the Al spectrum (STXM1), and the presence of diffraction peaks in Orion (ID22 XRD) suggest a mixture of spinel with a noncrystalline component. This is in agreement with the prior ID13 XRD report of sparsely distributed spinel crystallites in the original Orion particle (Gainsforth et al. 2014). We found the atomic ratio of Orion Al/Mg to be  $2 \pm 0.5$ , again consistent with  $\text{MgAl}_2\text{O}_4$ .

We estimated 12–20 fg Fe in Orion from the Fe stack, and a total-Fe map extracted from the stack (see Fig. 18) showed a seemingly unaltered Orion compared with the STXM1 Fe map (Fig. 10). The signal was too low for spectral interpretation, the result of our limiting photon fluence, high aerogel background, and dispersed Fe abundance (the brightest Fe spot in Orion contained 2 fg Fe). For comparison, we also show an XRF Fe map in Fig. 18, with Ni and Ca, from the ID13 analysis of the original Orion particle.

### STXM2 Characterization of Sirius

The PCA analysis yielded one spectral component in the STXM2 Mg XANES stack of the Sirius fragment labeled A in Fig. 14. The Mg spectrum of the large Sirius fragment was comparable to the small Sirius fragments in area B (Fig. 14). And these STXM2 Mg spectra of Sirius fragments were similar to the Sirius particle Mg spectrum taken before the ID22 analyses (during STXM1). We concluded that the result of the documented overexposure at ID22 was a physical dispersal of Sirius over 10  $\mu\text{m}$  of the track length, with some parts of Sirius contaminating Orion. We interpreted the STXM1 and STXM2 Sirius spectra together (Fig. 16).

We noted during STXM1 that the single-peak Sirius Mg spectrum did not match crystalline spinel, periclase, enstatite, or other clinopyroxenes. The Sirius

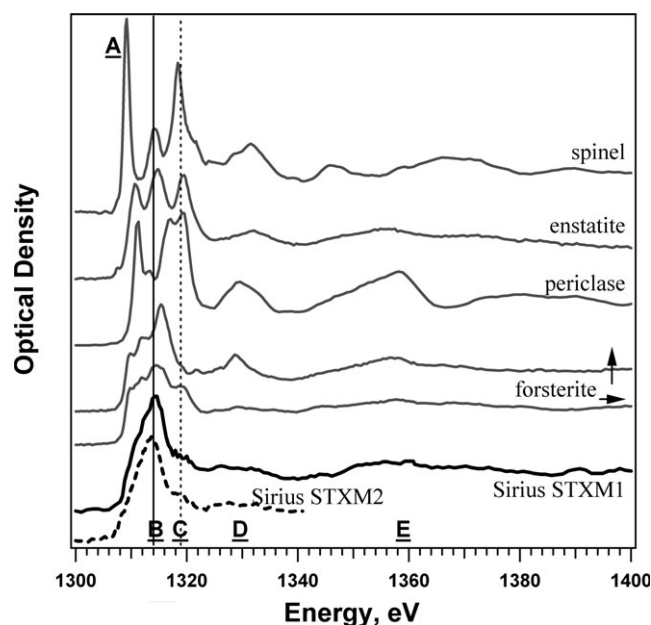


Fig. 16. Mg XANES spectra of Sirius acquired during STXM1 (black line) and STXM2 (dashed line), compared with those of spinel, enstatite, periclase, and forsterite with vertical ( $\uparrow$ ) and horizontal ( $\rightarrow$ ) polarized incident X-ray beams. Sirius spectrum maximum OD was 0.3, background aerogel OD was 0.6. The spectra were normalized at 1340 eV and vertical axis is in arbitrary units. Peak positions A to E labeled after Li et al. (1999).

spectrum was also a poor fit for olivine, but olivine (CN = 6) has an anisotropic crystalline structure so that crystal rotation alters the observed spectrum; periclase and spinel have cubic structure and their spectra are not affected by orientation. We demonstrated the effect on olivine by acquiring Mg spectra of exactly the same scan region of a forsterite standard, depicted by  $\rightarrow$  for horizontal X-ray polarization and  $\uparrow$  for vertical in

Fig. 16, to mimic crystal rotation. Peaks D and E, associated with long-range order (Ildefonse et al. 1995; Wu et al. 1996; Thompson 2008), were diminished in the horizontal polarization spectrum of the crystalline standard. Therefore, lack of Peaks D and E in Sirius was not sufficient to rule out olivine. The A-B-C triplet spectrum structure, associated with medium-range order (Wu et al. 1996), remained identifiable in our rotated crystalline standard spectra. The Sirius Mg spectrum, however, had a single, wide peak, with maximum at  $\approx 1314$  eV.

We ruled out amorphous  $\text{MgAl}_2\text{O}_4$  because spinel (CN = 4) structure is associated with a lower energy first peak ( $\approx 1309$  eV), and because Sirius did not contain Al. Comparing ID22 XRF element maps (Simionovici et al. 2014) with the STXM2 Mg map showed that the heavy elements (totaling  $<26$  fg) in Sirius did not correlate with Mg, and ID22 could not detect Si or O because of the background aerogel. We concluded that the Mg spectrum was most likely associated with a single Mg phase.

The Sirius Mg spectrum was consistent with modeled spectra of short-range order Mg–O (CN = 6,  $<5$  Å radii clusters) in periclase, forsterite, and enstatite predicted by full multiple scattering calculations (Wu et al. 1996; Cabaret et al. 1998; and Thompson 2008; respectively). Sirius was not consistent with the medium-range order modeled spectra (20 to 50 Å radii clusters), which do have the characteristic A-B-C triplets of each mineral, caused by interferences of multiscattering pathways from neighboring atoms. Randomly oriented CN = 6 Mg–O<sub>6</sub> units in polycrystalline silicates and glassy materials retain the identifiable A-B-C peak characteristics of their crystalline counterparts, albeit with broader and lower intensity peaks (Ildefonse et al. 1995; Thompson 2008).

The ID22 XRD analyses found Sirius fragments to be amorphous (Fig. 14); and because of the very similar Mg XANES spectra, we assumed that this result applies to all of the Sirius fragments and that the STXM1 Sirius particle was thus also amorphous. If the Mg–O clusters have approximately 5 Å radii, MgO and  $\text{Mg}_2\text{SiO}_4$  spectra would be degenerate, and we could not infer a composition of Sirius from its Mg XANES spectrum.

To investigate whether Sirius was a silicate or an oxide, we collected a Si K-edge XANES stack on the same Sirius fragment as the STXM2 Mg XANES stack (Fig. 17). Transmission at the Si K-edge through the 100  $\mu\text{m}$  thick picokeystone ( $27 \text{ mg cm}^{-3}$ ) was approximately 50%. We used the average intensities of the postedge (1848 to 1862 eV, avoiding the saturated 1847.5 eV  $\text{SiO}_2$  peak) and pre-edge (1832 to 1841 eV) to extract a Si map from the stack, and derived  $105 \pm 40$  fg Si for the Mg-rich region. For the same

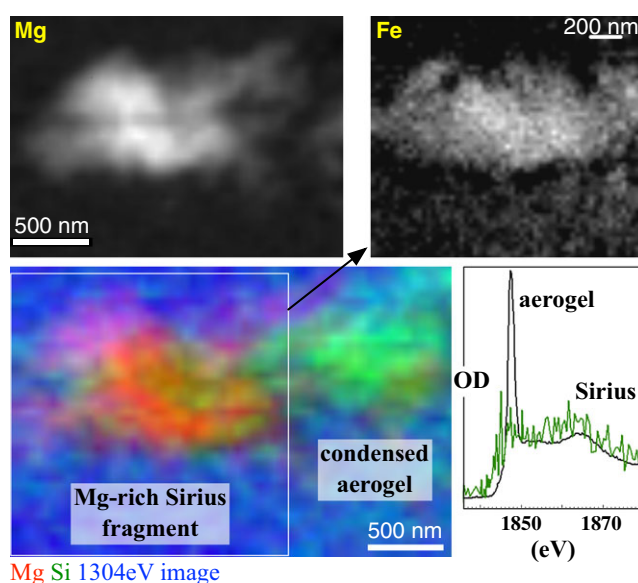


Fig. 17. Sirius fragment during STXM2. Clockwise: Mg map from the Mg stack (Region A, Fig. 14), Fe map from the Fe stack; Si spectrum (OD 0.12 above Track 30 aerogel OD 0.6) normalized to an aerogel spectrum, with arbitrary OD shown on the vertical axis; combined Mg map subregion from Fig. 14 (red), Si map from Si X-ray absorption near-edge structure stack (green), and 1304 eV absorption image (blue). The area of the Fe stack is marked on the RGB map. (see online version for color figure.)

region, Mg mass was  $155 \pm 30$  fg. The neighboring condensed aerogel particle contained  $600 \pm 70$  fg Si above background aerogel. We estimated a Mg/Si ratio of approximately 1.7. We conclude that Si correlated with Mg is evidence that Sirius was more likely a silicate rather than an oxide.

#### Interpretation of I1043,1,30 (Track 30) Results

We combined evidence from XRF, XRD (Brenker et al. 2014; Gainsforth et al. 2014; Simionovici et al. 2014) with STXM measurements to reconstruct the characteristics of the Track 30 impactor particle, Orion.

The presence of a second particle in the first round of the STXM1 analyses was unexpected, as only one particle had been detected in the XRF maps produced at ID13. Sirius was located 3  $\mu\text{m}$  from Orion, center to center, and the depth of focus was approximately 1.5  $\mu\text{m}$  in 0.7 keV images. Orion and Sirius were therefore too far apart to have overlapped in the ID13 XRF maps, when the picokeystone was viewed at  $45^\circ$ .

The observation, at the start of STXM1, of a dark crack in the center of the Track 30 was also unexpected. We found (during STXM2) that the crack, 30  $\mu\text{m}$  length of track, and the aerogel around Orion (approximately 5  $\mu\text{m}$  radius) contained 550–2200 fg Fe; less than 30 fg Fe was present in Orion. In contrast,



Brenker et al. (2014) detected  $840 \pm 100$  fg Fe in the original Orion particle; there was no Fe-filled crack and no Fe elsewhere in the track according to ID13 XRF data. We concluded that the total Fe detected in Track 30 by STXM was consistent with the previous quantity of Fe measured by ID13 XRF, but approximately 96% of the Fe from Orion had been redistributed into the track aerogel before the STXM1 analyses.

In addition to the Fe maps, Al and Mg maps of the track region taken during STXM1 showed that it was predominantly Fe that moved out of Orion and into the surrounding aerogel, leaving Al in Orion, and Mg in the Orion and Sirius particles (Fig. 13). This suggests that Fe originally present in Orion was in a different phase from Mg and Al.

In Orion, a single component Mg XANES spectrum with broad, low-intensity peaks matched a spinel-like structure, which was mostly amorphous. Maps of  $200 \pm 40$  fg Mg and  $425 \pm 25$  fg Al were spatially correlated, and the single Al XANES spectrum also supported an amorphous spinel-like structure, at least in part. ID13 XRD analyses detected sparse spinel crystallites, but ID13 XRF could not detect Mg or Al and the Mg-Al amorphous phase was not visible with XRD. STXM was the only technique used in ISPE able to detect an amorphous Mg-Al-O phase.

We conclude that  $\text{MgAl}_2\text{O}_4$  spinel was present in the pristine Orion particle, analyzed by ESRF ID13, and this radiation-hard material was less affected by the modifying event, which displaced the olivine and Fe phase. As we found no Al in Sirius, and  $<50$  fg Al associated with the redistributed Fe, we conclude that the surviving Al phase in Orion accounts for  $>90\%$  total Al of the original particle,  $475 \pm 35$  fg Al. The XRF map of Fe, Ni, Ca from ID13 (Fig. 18) shows Ca, which could be associated with an Al phase, but the morphology of the particle was changed so that we could not identify a correlation between Al and Ca.

ID13 XRD analyses detected a strong olivine signal in the center of Orion, but no olivine diffraction was observed in Orion or Sirius in the subsequent ID22 XRD data. The loss of the crystalline olivine signal in Orion was not the result of amorphization of olivine in place, because we detected a total-Mg depletion instead of evidence of amorphous silicate using Mg XANES spectroscopy, which is sensitive to amorphous Mg phases ( $>20$  fg  $\mu\text{m}^{-2}$  Mg). We concluded that the Mg originally present in olivine was entirely lost from Orion.

Our assertion that Sirius was amorphous, before and after the disruption at ID22, was drawn from two lines of evidence: (1) ID22 XRD results showed that Mg-rich Sirius fragments within the scan range were amorphous, and we applied those results to all of the

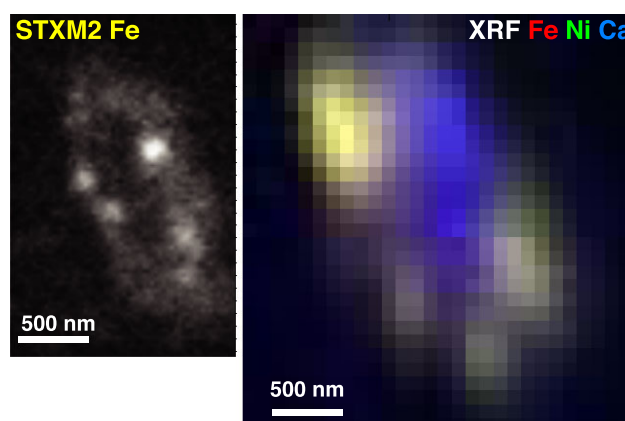


Fig. 18. Left, Fe map of Orion after ID22 XRF analysis (STXM2). Right, prior to STXM1 Fe, Ni, Ca XRF map of Orion from ESRF ID13 (Brenker et al. 2014).

spectrally similar Sirius fragments (STXM2) and the Sirius particle (STXM1), and (2) the Mg XANES spectrum has no A-B-C triplet structure. Glasses have the triplet structure in their Mg XANES spectra, because they have medium-range order, but they may lack EXAFS peaks D and E because they lack long-range order. Furthermore, silicate glasses will have randomly oriented Mg-O cluster units, similar to polycrystalline silicates, and yet the spectral A-B-C identity is still visible, albeit broader than for a single crystal. We concluded that Sirius was highly amorphous, exhibiting minimal medium-range order. We measured  $300 \pm 60$  fg Mg diluted to very low density (approximately  $0.2 \text{ g cm}^{-3}$ ) and noted very low Fe content ( $<10$  fg Fe) during STXM1; Simionovici et al. (2014) reported  $4.4 \pm 0.5$  fg Fe in Sirius from XRF. We could not infer a probable composition from the single-peak Mg spectrum, but Si mapping of a Mg-rich Sirius fragment (during STXM2) provided some evidence that the major component of Sirius could have been an amorphous Mg silicate phase.

The lack of observed olivine and the loss of most of the originally observed Fe from Orion indirectly imply that the existence of Sirius was itself the result of the undocumented modifying event that occurred before STXM1, and was not a surviving phase of the pristine particle or a result of capture effects. By mapping Mg before and after the X-ray overexposure at ESRF ID22, we found that the main Mg-rich fragment of Sirius had moved  $5 \mu\text{m}$  up the track; Simionovici et al. (2014) detected no further alteration to the Orion remnant. It is plausible that the event that resulted in 96% loss of Fe from Orion also resulted in the loss of forsterite from Orion and formation of amorphous Sirius  $3 \mu\text{m}$  away, i.e., the original olivine had very little fayalite content. A sphere of forsterite (assuming  $3.3 \text{ g cm}^{-3}$  nonporous density) containing 300 fg Mg would have a



diameter 0.85  $\mu\text{m}$ , which is consistent with the XRD topographs from ID13 placing olivine at the center of Orion (Gainsforth et al. 2014). If Sirius did originate as the olivine in Orion observed by ID13 XRD analysis, the total Mg in Orion (as captured) was the sum of remnant Orion Mg plus Sirius,  $\text{Mg} = 500 \pm 70 \text{ fg}$ .

During STXM2, we also detected low-intensity Ni in the crack region and in Sirius, which we attributed to Ni loss from Orion. Simionovici et al. (2014) reported an enhanced  $\text{Ni}/\text{Fe} = 4$  in Sirius compared with Orion  $\text{Ni}/\text{Fe} = 0.07$  (no  $\text{Ni}/\text{Fe}$  measurement was made on the crack region). STXM2 maps showed that Ni was correlated more closely with Mg-rich particles than with redispersed Fe (Fig. 14), perhaps forming a coating on the fragments. It is not clear whether the Sirius Fe-Ni chemically separated during the overexposure at ID22, or whether Ni was originally present spanning different phases, with most Ni associated with the 96% Fe phase lost from Orion before STXM1, and a minor Ni component remaining associated with the Mg phases in Sirius ( $\text{Ni}/\text{Mg} = 0.02 \pm 20\%$ ) and Orion ( $\text{Ni}/\text{Mg} 0.005 \pm 20\%$ ).

Assuming that these conclusions are correct, we can summarize the major components of original Orion, allowing for the unknown Fe oxidation state and phase. If Fe was present as Fe and/or FeO, the major phases were (by molar fraction)  $19 \pm 3\% \text{ Mg}_2\text{SiO}_4 + 27 \pm 2\% \text{ MgAl}_2\text{O}_4 + 45 \pm 3\% \text{ Fe}/\text{FeO} + 9\%$  minor phases; if Fe was more oxidized, the components could be  $\sim 26 \pm 3\% \text{ Mg}_2\text{SiO}_4 + \sim 37 \pm 3\% \text{ MgAl}_2\text{O}_4 + \sim 25 \pm 5\% \text{ Fe}_2\text{O}_3/\text{Fe}_3\text{O}_4/\text{Fe}_2\text{SiO}_4 + \sim 12\%$  minor phases. The total mass of Orion from the combination of all measured elements (Table 3) was  $(3.1\text{--}3.8) \pm 0.4 \text{ pg}$ , allowing for a range of stoichiometric Si and O in the Fe phase. Minor metals were included in the total as oxides (combined 7 mol%). The error is the sum of elements' measurement errors. An additional  $\pm 10\%$  systematic error is due to uncertainties in the X-ray absorption cross sections. Sulfur could account for  $\leq 6\%$  Fe phase (Brenker et al. 2014), and is within the total mass error.

We estimated the volume from  $V = 4A^{3/2}/(3\sqrt{\text{II}}) = 4.5 \mu\text{m}^3$  where the area  $A$  is estimated from the ID13 XRF maps, as being most representative of Orion as captured. With this assumption, the density of Orion was  $0.7 \text{ g cm}^{-3}$ . We have no information regarding amorphous C content, which would increase the density if present interstitially. Even allowing for a significant carbonaceous component, Orion appears to have originally been a coherent, but low-density, multiphase object. We have ruled out terrestrial contamination because the particle was clearly associated with an impact track. We have also

ruled out a spacecraft origin, because the composition is different from the Stardust SRC deck, which was the only part of the spacecraft consistent with the particle's trajectory.

### *Assessment of Possibility of Beam Damage at ALS 11.0.2*

The reconstruction of Orion's composition was complicated principally by a modifying event that occurred before the first STXM analyses on ALS 11.0.2. The last XRF maps collected during the ESRF ID13 analyses show no change to Orion, but the images from STXM1 showed an altered morphology, which then remained constant throughout the remaining STXM analyses. To investigate the timing of the modifying event, we returned to the first STXM images we acquired on 11.0.2 after the ID13 analyses. These images were coarse navigation images taken before any focusing on the keystone.

We have considered a possible failure mode at ALS 11.0.2 that could have accidentally irradiated Track 30. White beam irradiation was quickly ruled out. We considered monochromatic beam irradiation for 20 min during the He purge of the STXM chamber, when the sample was in position with the beam lockouts enabled, but we did not collect any data. We did record the Z-axis position of the zone plate during the first 1000 eV navigation image of the sample, which turned out to be 400  $\mu\text{m}$  out of focus of Orion. We calculated the beam radius at this distance to be 10  $\mu\text{m}$ , from the trigonometry defined by the zone plate (Equation 6 gives focal distance = 4840  $\mu\text{m}$ , where  $D = 240 \mu\text{m}$ ,  $\delta_{\text{rN}} = 25 \text{ nm}$ , and  $\lambda = 1.24 \text{ nm}$  at 1000 eV). The beam was set to  $1 \times 10^7 \text{ counts/s}$ , which is equivalent to a flux of  $3.2 \times 10^{12} \text{ ph s}^{-1} \text{ cm}^{-2}$  for a 10  $\mu\text{m}$  radius beam. If the beam had been left directly on Orion for 20 minutes, the total photon fluence would have been approximately  $4 \times 10^{15} \text{ ph cm}^{-2}$  (ignoring absorption by air, the 50 nm thick silicon nitride membrane, and aerogel), which is about the same fluence as the (in focus) Orion Al XANES stack, which we have shown to be safe from radiation damage. The sample stage's center position for this first-light navigation image was  $(X + 20, Y + 50) \mu\text{m}$  from the eventual location of the Orion particle, which was most likely also the position of the parked beam during the He purge phase. So, even if this accidental irradiation had occurred, the 10  $\mu\text{m}$  beam would have missed Orion. Thus, while we are confident that the STXM analyses of I1043,1,30 proceeded without errors, with no accidental irradiation, we have shown that an unmonitored STXM beam could not have in any case caused the removal of Fe from Orion, nor the destruction of olivine.

Circumstantial evidence suggests that the modification of Orion occurred before the Track 30

Table 3. Combination of elements in Orion-as-captured from STXM and XRF.

Element	Measured mass, fg	Element total, femtomole	Oxide	Molar oxides, femtomole
Mg	300 ± 60 in Mg <sub>2</sub> SiO <sub>4</sub> 200 ± 40 in MgAl <sub>2</sub> O <sub>4</sub>	20.6 ± 2.9	MgO	12.3 8.2
Al	475 ± 35	17.6 ± 1.3	Al <sub>2</sub> O <sub>3</sub>	8.8
Ca <sup>a</sup>	16 ± 2	0.57 ± 0.06	CaO	0.6
Cr <sup>a</sup>	12 ± 1	0.23 ± 0.02	Cr <sub>2</sub> O <sub>3</sub>	0.1
Mn <sup>a</sup>	15 ± 1	0.25 ± 0.03	MnO	0.3
Fe <sup>a</sup>	840 ± 100	15.0 ± 1.8	Fe <sup>b</sup>	15.0
Ni <sup>a</sup>	55 ± 6	0.94 ± 0.09	NiO	0.9
Cu <sup>a</sup>	10 ± 1	0.17 ± 0.02	CuO	0.2
Si <sup>b</sup>	175–385	6.2–13.7	SiO <sub>2</sub>	6.2–13.7
O <sup>b</sup>	970–1430	61–90		
Total	3090 ± 450 + (Si,O) <sub>Fe</sub>			

STXM = Scanning transmission X-ray microscopy; XRF = X-ray fluorescence.

<sup>a</sup>XRF measurements (Brenker et al. 2014).

<sup>b</sup>Stoichiometric Si and O from forsterite, oxides, and varying the Fe phase Fe, FeO, Fe<sub>2</sub>O<sub>3</sub> and Fe<sub>2</sub>SiO<sub>4</sub>.

picokeystone arrived back in Berkeley. The silicon nitride windows were concave before STXM1 analyses, but they had been flat when the sample was originally mounted. The silicon nitride sandwich assembly opened and was safely reattached before the later ID22 analyses and the membrane shape remained, which ruled out a pressure differential as cause. No other membranes were altered in this way after shipping or after any STXM, XRF, or XRD analyses during ISPE, including the highest recorded fluence XRD analyses of I1047,1,34 (Track 34, Hylabrook). The final XRF maps of Orion taken after the XRD analyses at ID13 showed no change in morphology or loss of iron.

Thermal disintegration of olivine and the Fe phase in Orion was unlikely, because it would have required temperatures >1000 °C, but we found that the rest of the keystone and the silicon nitride membrane assembly had remained intact. The cause of the modification to Orion remains a mystery.

The overexposure at ID22, causing a second modification to the sample, had minor negative effects on the overall interpretation of the characterization of Track 30. STXM Mg analyses had to be considered in the context of the ID22 overexposure, and Si XANES data were only collected on Sirius fragments after the ID22 analyses, so they were not quantitative for Sirius. We did gain useful information; however, for example, Mg, Fe, and Ni element maps of Sirius during STXM1 and the early ID22 maps showed that these elements appeared to be correlated in Sirius at the start of the ID22 run, but Fe decoupled from Mg after the overexposure, suggesting that Fe and Mg were present in different chemical phases. The combined dose history experienced during the XRF, XRD, and STXM analyses by the particles in Track 30 is shown in Fig. 19.

### I1047,1,34 (Track 34, Hylabrook)

Track 34 was discovered through Stardust@home and named Hylabrook by its first discoverer, Naomi Wordsworth. The 57 µm long track was extracted in an 85 µm thick picokeystone, which became slightly compacted during mounting in the silicon nitride window sandwich, making the track bend by about 20°. Track 34 was analyzed first by STXM (“STXM1”), next by XRF/XRD at ESRF beamline ID13, then by further STXM analyses (“STXM2”), summarized in Table 4.

#### STXM1: Pre-ID13 Analysis of Hylabrook

The aerogel density in I1047,1,34 was high and variable,  $48 \pm 12 \text{ mg cm}^{-3}$  (derived from a 1314 eV image of the picokeystone, assuming 85 µm aerogel thickness), with the densest region around the terminal particle. Transmission at 700 eV was only 5%, limiting Fe analyses, and precluding the possibility of C XANES measurements.

We mapped Mg in the track, and found one Mg-rich particle, Hylabrook, which comprised an approximately 1 µm diameter core surrounded by a 3 µm diameter halo. Fe was below detection limit ( $<200 \text{ fg } \mu\text{m}^{-2}$ ), where OD was 3.2 (4% transmission). Ce and Ni were also below detection limits ( $<15 \text{ fg } \mu\text{m}^{-2}$  for both), but the 850 to 880 eV images provided high-contrast images of the track, with approximately 15% transmission. These images verified that Hylabrook was associated with an impact track, and that subsequent analyses were made on the terminal particle. We mapped Al at 1561 eV (Al metal) and 1568 eV and found  $\approx 40 \text{ fg}$  oxidized Al. We detected a second particle, but determined that its focal depth was 25 µm below the track. The track diameter was  $\approx 1 \text{ } \mu\text{m}$ .

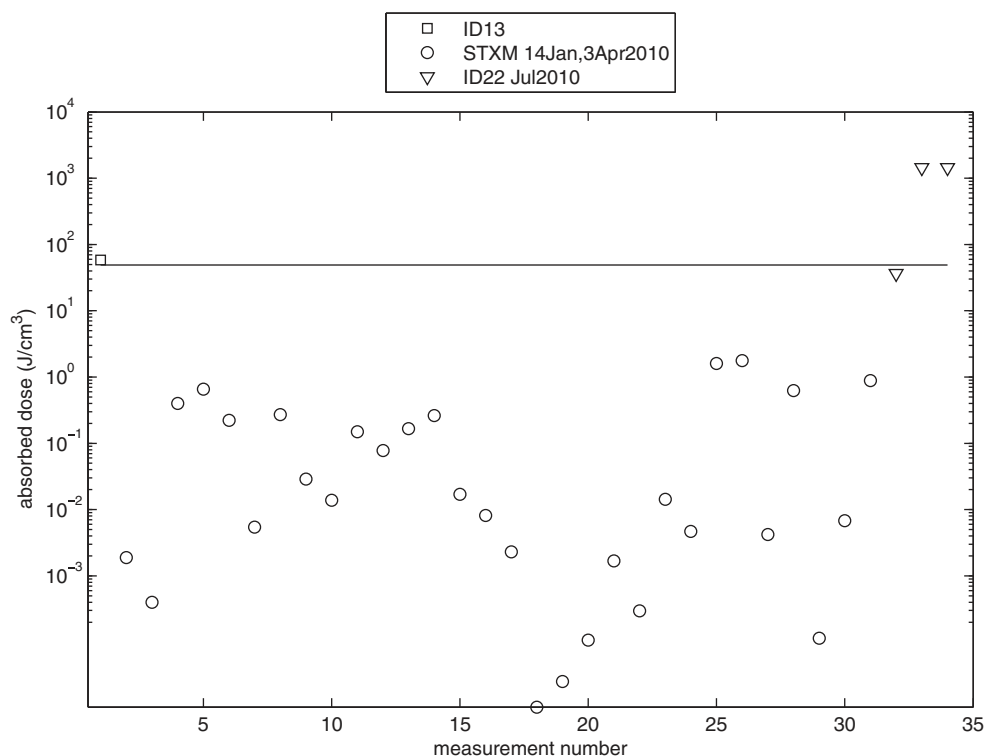


Fig. 19. Analytical X-ray absorbed dose for analyses of Orion, versus analysis sequence. Summed SXRF/SXRD analyses at ID13 at ESRF (square), individual STXM1 analyses (circles), and SXRF/SXRD analyses at ID22 at ESRF (triangles). STXM2 doses (not shown) are similar to STXM1 analyses. The horizontal line is the ISPE self-imposed limit based on expected interstellar irradiation (Gruber et al. 1999).

Table 4. STXM analyses of I1047,1,34.

Measurement	Pixel size ( <i>X</i> , <i>Y</i> )	Dwell per pixel	Quantification	Result, reference
<i>STXM1</i>				
Mg map	80 nm	1 ms		
Fe map	50 nm	10 ms	Fe inconclusive (OD = 3.2)	Sample too thick.
Ce map	40 nm	2 ms	n.d.	
Ni map	40 nm	2 ms	n.d.	
Al maps	40 nm	2 ms	40 fg Al ( $\pm 90\%$ )	Rim of particle
Si map	80 nm	2 ms	380 $\pm$ 100 fg Si	Si map
Mg stack	75 nm	1 ms	655 $\pm$ 70 fg Mg	97% olivine
<i>XRF/XRD at ESRF ID13</i>				
			1300 $\pm$ 100 fg Fe	Brenker et al. (2014)
<i>STXM2</i>				
Mg stack	100 nm	0.8 ms	625 $\pm$ 70 fg Mg	50% olivine
Al stack	60 nm	3 ms	40 fg Al in halo ( $\pm 90\%$ )	Al, not metal
Si stack	60 nm	1 ms		Core and halo
Fe map	40 nm	40 ms	150–2000 fg Fe	
Mg map	25 nm	2 ms	n.d.	2nd particle near track
880 eV	133 nm	1 ms		Fig. 24

STXM = scanning transmission X-ray microscopy; XRF = X-ray fluorescence; XRD = X-ray diffraction.

near the aerogel surface, widening to 2  $\mu\text{m}$  near Hylabrook.

We collected a 75 nm pixel Mg XANES stack, from which we calculated a total mass of 655  $\pm$  70 fg of Mg.

We estimated 380  $\pm$  100 fg of Si from a Si map. In Fig. 20, we show Mg, Al, and Si maps of Hylabrook. Si appeared to be native to the particle, correlated with Mg in both the core and halo (Si did not merely appear



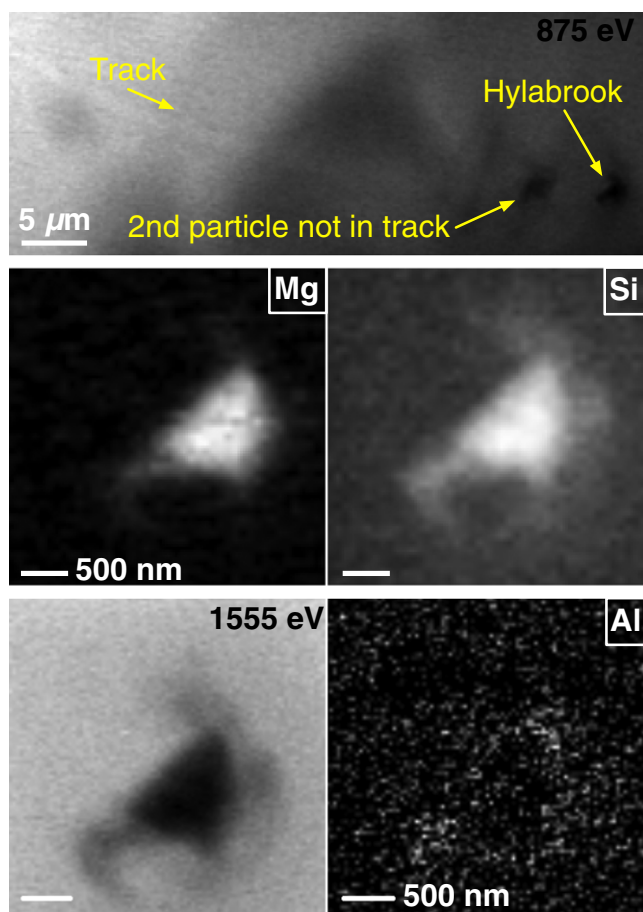


Fig. 20. I1047,1,34 track and terminal particle (Hylabrook) before ESRF ID13 XRF analyses (STXM1). Top, 875 eV absorption image, shows the curved track due to a distortion in the aerogel picokeystone during mounting. Middle, aligned Mg and Si maps. Bottom, aligned 1555 eV absorption image and Al map.

as a shell of aerogel). Al was present on the particle rim.

PCA analysis of the Mg XANES stack showed two spectral components representing the core (97% Mg) of the particle and the low-density halo (3% Mg). The Mg XANES spectrum for the Hylabrook dense core is a reasonable match to olivine (see Fig. 22), but with broader, weaker peaks. As olivine is anisotropic, the crystal orientation, the number of grains, and the degree of disorder make an exact match of the Hylabrook spectrum to the forsterite standard unlikely.

After STXM1, the ISPE team collected XRF and XRD data on Hylabrook on ID13 at ESRF. Brenker et al. (2014) report finding two particles in I1047,1,34 and Gainsforth et al. (2014) report olivine diffraction located in Hylabrook particle core. The ID13 analyses were successful, but the X-ray fluences experienced by

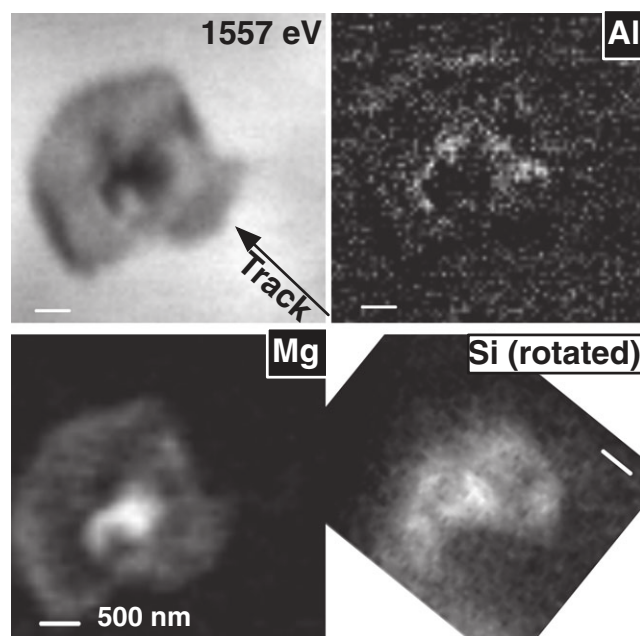


Fig. 21. Analyses after disruption of Hylabrook due to overexposure on ESRF ID13. Clockwise, a 1557 eV image showing orientation of the track, maps of Al, Si (rotated) and total-Mg.

the sample significantly exceeded the dose limits imposed by the ISPE team (see Fig. 26).

#### Post-ID13 Analysis of Hylabrook (STXM2)

After Track 34 was analyzed at ESRF ID13, we acquired Mg, Al, Fe, and Si stacks on Hylabrook. The Si and Fe maps were taken in a different orientation because the keystone moved within its  $\text{Si}_3\text{N}_4$  membrane mount. Mg, Al, Si, and Fe maps are shown in Fig. 21.

PCA component Mg XANES spectra revealed  $315 \pm 70$  fg olivine-like Mg in the Hylabrook core and  $350 \pm 70$  fg amorphous Mg in the halo. We compared Mg spectra (Fig. 22) and Mg component maps (Fig. 23) from stacks acquired during STXM1 and STXM2. After overexposure at ID13, the Mg abundance of the olivine-like core had decreased from 97 to 47%, the amorphous halo increased to 53%, while the total Mg was not significantly changed. We concluded that olivine had undergone a partial amorphization and displacement.

The Al XANES stack confirmed the presence of  $\approx 40$  fg Al in the halo, but not in the core. The peak was around 1568 eV, consistent with an alumina phase (not corundum), although the weak spectrum was too noisy to infer structure or order. The alumina appeared to exist as a rim on the original olivine core.

The STXM2 Si map shown in Fig. 21 was produced from the Si stack by averaging  $\Delta\text{OD}$  ( $\approx 0.5$

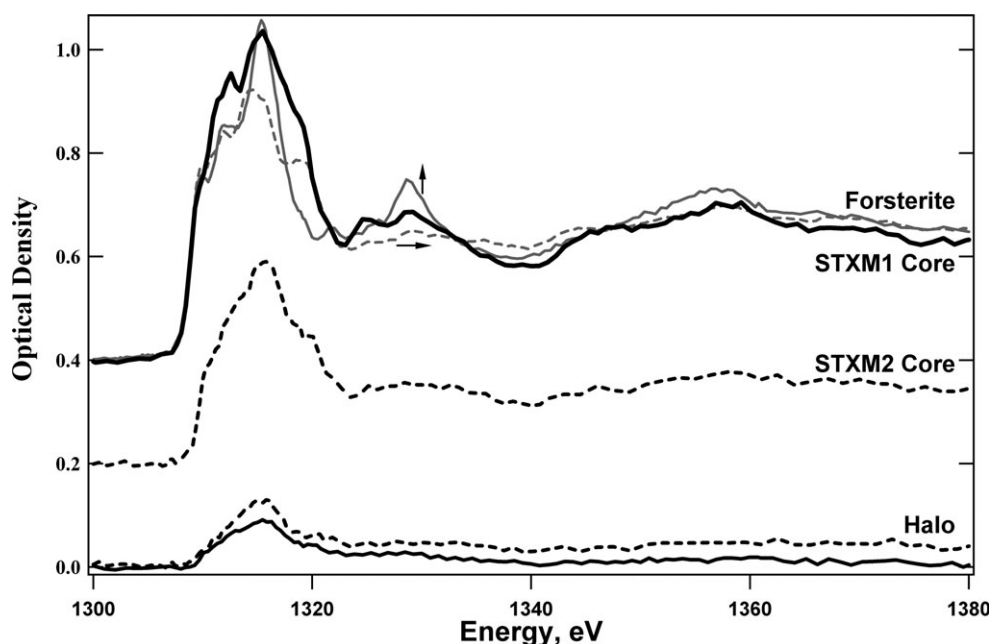
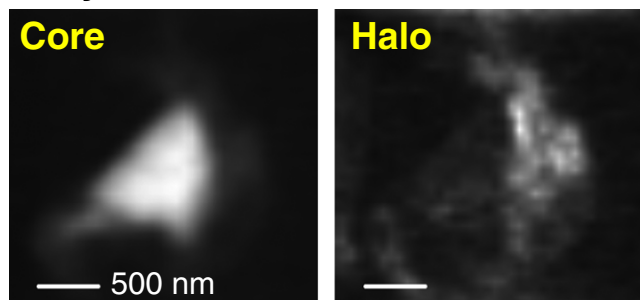


Fig. 22. Mg XANES spectra of I1037,1,34 Hylabrook, offset for clarity. Hylabrook core during STXM1 (black line) before the ESRF ID13 analyses, with forsterite spectra acquired using vertical (gray line) and horizontal (gray dashed line) incident beam polarization, normalized to Hylabrook STXM1 Core intensity at 1350 eV. Hylabrook STXM1 Halo (black line) accounts for approximately 3% STXM1 total  $655 \pm 70$  fg Mg. STXM2 component spectra (black dashed lines) are similar to STXM1 components in shape, but they differ in intensity: STXM2 Core decreased to 47% and STXM2 Halo increased to 53% of total  $625 \pm 70$  fg Mg.

### Hylabrook STXM 1 Before ID13



### Hylabrook STXM 2 After ID13

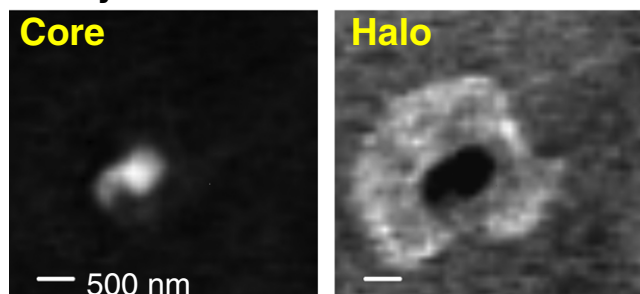


Fig. 23. I1047,1,34 maps of Mg X-ray absorption near-edge structure component spectra representing olivine-like core and amorphous halo in Hylabrook, before ESRF ID13 XRD analyses (STXM1) and after (STXM2).

above aerogel background OD of 0.8) between 1852 and 1865 eV, avoiding the oversaturated peak at approximately 1847 eV from the dense Si-rich particle core area.

The high OD of aerogel in this sample ( $OD = 3.2$  at 710 eV) introduced very large systematic errors in the direct measurement of Fe: we derived 150–2000 fg Fe, which was consistent with  $1300 \pm 100$  fg Fe from XRF observations at ID13 (Brenker et al. 2014). However, Mg analyses of Hylabrook demonstrated partial amorphization of olivine and dispersion of mass after the ESRF ID13 XRF/XRD analyses, which was reminiscent of the I1043,1,30 Orion modification. In an effort to improve the precision of the STXM Fe measurement, we investigated the possibility of Fe loss using an indirect method. We compared a normalized absorption image of Hylabrook acquired at 850 eV before the ID13 analyses (STXM1) with another image acquired at 880 eV after ID13 analyses (STXM2), shown in Fig. 24.

The measured OD of each pixel (normalizing to background aerogel) was the sum of OD contributions from every species present (Equation 2). We estimated that Hylabrook-STXM1 had an average OD of 0.8 at 850 eV in a  $6.6 \mu\text{m}^2$  area, and that Hylabrook-STXM2 had an average OD of 0.6 at 880 eV in a  $7.6 \mu\text{m}^2$  area.

Table 5. Combination of bulk major elements in I1047,1,34 from STXM and XRF.

Element <sup>a,b</sup>	Measured mass, fg	Element total, femtomole	Oxides	Oxide fraction (e.g., FeO) <sup>c</sup>
Mg	655 ± 70	26.9 ± 2.9	MgO	38%
Al	40 ± 20	1.5 ± 0.7	Al <sub>2</sub> O <sub>3</sub>	1%
Si	380 ± 100	13.5 ± 3.6	SiO <sub>2</sub>	19%
Ca <sup>a</sup>	8 ± 10%	0.2 ± 10%	CaO	0.3%
Cr <sup>a</sup>	362 ± 10%	7.0 ± 10%	Cr <sub>2</sub> O <sub>3</sub>	5%
Mn <sup>a</sup>	111 ± 10%	2.0 ± 10%	MnO	3%
Fe <sup>a</sup>	1300 ± 100	23.3 ± 1.8	FeO <sup>c</sup>	33%
Ni <sup>a</sup>	4 ± 10%	0.07 ± 10%	NiO	0.1%
Cu <sup>a</sup>	3 ± 10%	0.04 ± 10%	CuO	0.1%
O <sup>b</sup>	900–1700			
Total	(3960–4520)±340			100%

STXM = scanning transmission X-ray microscopy; XRF = X-ray fluorescence.

<sup>a</sup>XRF abundance measurement (Brenker et al. 2014)

<sup>b</sup>Stoichiometric O varied with Fe phase (Fe, FeO, or Fe<sub>2</sub>O<sub>3</sub>) to compute a total mass range.

<sup>c</sup>The Fe phase is unknown. We used FeO to show one possible oxide mole fraction set.

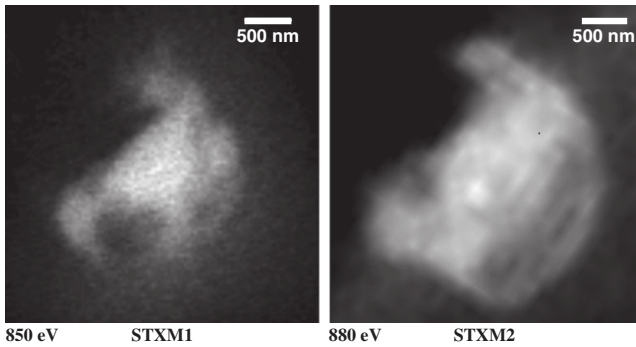


Fig. 24. Optical density maps of Hylabrook created by normalizing single energy images to background aerogel. Left, average optical density (OD) = 0.8 of 6.6  $\mu\text{m}^2$  particle before ID13 analyses (40 nm pixels). Right, average OD = 0.6 of 7.6  $\mu\text{m}^2$  particle (133 nm pixels).

The main contributions to OD in this energy range are from the tail of O K-edge and the L-edges of transition metals Fe, Cr, Mn, and Ni (above 853 eV, STXM2 only). We assumed that Hylabrook comprised two components, 1896 fg of Mg<sub>2</sub>SiO<sub>4</sub> and metal oxides (1673 fg FeO, 560 fg Cr<sub>2</sub>O<sub>3</sub>, 162 fg MnO, and 5 fg NiO), using metal abundances from ID13 XRF (Brenker et al. 2014) in Table 5. We ignored possible transition metal silicates, because Si was too low to allow the majority of metals to be silicates.

We plotted in the calculated OD curves (Fig. 25) for the dense Mg<sub>2</sub>SiO<sub>4</sub> Hylabrook-STXM1 core (1.3  $\mu\text{m}^2$ ,  $1.4 \times 10^{-4}$  g cm<sup>-2</sup>), the redistributed STXM2 Mg<sub>2</sub>SiO<sub>4</sub> (7.6  $\mu\text{m}^2$ ,  $2.5 \times 10^{-5}$  g cm<sup>-2</sup>), and for the combined metal oxides (7.6  $\mu\text{m}^2$ ). The measured OD was higher than would be expected for forsterite alone: in STXM1, it was higher than the dense Mg<sub>2</sub>SiO<sub>4</sub> core, and in STXM2, the measured OD was approximately

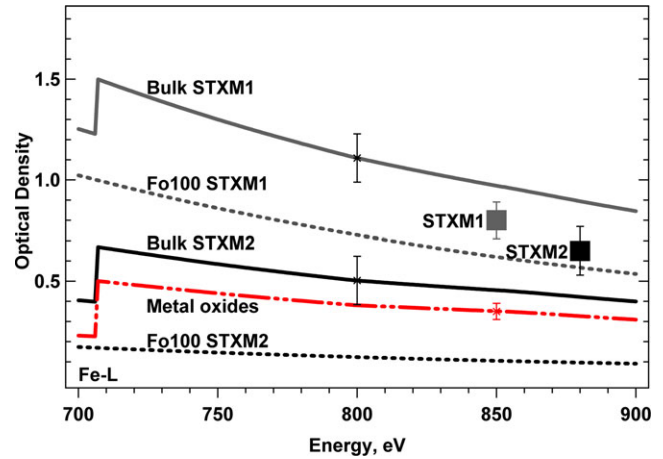


Fig. 25. Plot of calculated OD spectra for I1047,1,34 using elemental abundances (this work and Brenker et al. 2014) compiled in Table 5, and measured areas (Fig. 24). Metal oxides 7.6  $\mu\text{m}^2$ ,  $3.2 \times 10^{-5}$  g cm<sup>-2</sup> (23FeO 3MnO 4Cr<sub>2</sub>O<sub>3</sub> 0.1NiO) were assumed to be the same for STXM1 and STXM2 (red - -), the error bar represents uncertainty in (FeO + Fe)/ΣFe. STXM1 Core of 1.3  $\mu\text{m}^2$ ,  $1.4 \times 10^{-4}$  g cm<sup>-2</sup> Mg<sub>2</sub>SiO<sub>4</sub> (gray dash); bulk STXM1 (solid gray) is the sum of the STXM1 core and metal oxides curves, which is consistent with measured STXM1 optical density (OD) (gray square). STXM2 7.6  $\mu\text{m}^2$ ,  $2.5 \times 10^{-5}$  g cm<sup>-2</sup> Mg<sub>2</sub>SiO<sub>4</sub> (black dash); bulk STXM2 (solid black) is the sum of STXM2 Mg<sub>2</sub>SiO<sub>4</sub> and metal oxides, which is consistent with measured STXM2 OD (black square). Bulk errors are estimated from uncertainties in abundances and measurement of area.

six times higher than the redistributed Mg<sub>2</sub>SiO<sub>4</sub>. The measured OD values fit best to the sum of forsteritic- and metal oxide compositions. Estimated errors, ±20%, are much larger than element quantification across an edge jump, because we can only model total OD. Nevertheless, we conclude that we have no evidence for loss of Fe during ID13 analyses of Hylabrook.



Without reliable direct STXM evidence for Fe, Cr, Mn, or Ni, these comparisons provide a valid comparison with XRF data. Metal oxides/silicates were sufficient to produce the high measured OD at 880 eV, but large errors could encompass Fe metal. The density of metal oxides was evenly distributed over the entire disrupted particle, and not correlated with the remaining olivine core. A plausible, but not exclusive, fit for STXM1 Hylabrook (850 eV image) was a forsteritic particle core (OD 0.53) plus Fe (OD 0.26), with minor OD contribution from  $\text{Cr}_2\text{O}_3$  and MnO.

### *Interpretation of I1047,1,34 Results*

The STXM1 Mg XANES data are consistent with the XRD observations of Hylabrook, which give, independently, an excellent fit to olivine (Gainsforth et al. 2014). Post-ID13 imaging by STXM showed a partial amorphization of olivine and redistribution of the resulting amorphous silicate. XRF results included the detection of major elements Fe, Cr, and Mn (Brenker et al. 2014); we were not able to directly measure these metals by STXM due to the high absorbance of the aerogel in the energy range of the Fe, Cr, and Mn L-edges.

Si and Mg were correlated before the ID13 analyses (Fig. 20) consistent with an olivine core and an amorphous Mg-bearing silicate halo. After the ID13 analyses, the total mass of Mg remained constant, but the olivine component decreased while the amorphous Mg component increased; and the STXM2 amorphous Mg-silicate component spectrum is comparable to the STXM1 Mg halo spectrum. Apparently, olivine was amorphized, which also indirectly suggests that the Mg-bearing halo component was amorphous silicate with forsteritic composition. The bulk atomic Mg/Si ratio in Hylabrook was  $2.0 \pm 0.4$ , which could allow up to 30% of total Fe to be present as a silicate ( $\text{Fo} > 79$ ). We noted that Fe and Mg were not well correlated after the particle disruption, which was further evidence that the majority of Fe was not present in the olivine phase. We conclude that the original Hylabrook particle composition was Fo-rich olivine (in agreement with XRD results) surrounded by Fe, Cr, Mn, and Al amorphous phases.

We combined the masses of elements measured by STXM and XRF (Brenker et al. 2014) in Table 5. If the Fe phase was Fe and/or FeO, the major phases could be 31%  $\text{Mg}_2\text{SiO}_4$  + 54% Fe/FeO + 8%  $\text{Cr}_2\text{O}_3$  + 5% MnO + 2% (Ca, Al) oxides; if the Fe phase was  $\text{Fe}_2\text{O}_3$ , the components could be 43%  $\text{Mg}_2\text{SiO}_4$  + 37%  $\text{Fe}_2\text{O}_3$  + 11%  $\text{Cr}_2\text{O}_3$  + 6% MnO + 3% (Ca, Al) oxides. The total mass of Hylabrook was  $(4.0\text{--}4.5) \pm 0.4$  pg, allowing for the range of stoichiometric O in the Fe phase. The error is the sum of elements' measurement

errors. There is an additional 10% systematic error due to uncertainties in the X-ray absorption cross sections.

The volume of Hylabrook-as-captured (STXM1) was  $12.8 \mu\text{m}^3$ , resulting in a particle density  $0.33 \pm 0.02 \text{ g cm}^{-3}$ . The track diameter near the aerogel surface was  $2 \mu\text{m}$ , equivalent to a  $4.2 \mu\text{m}^3$  sphere, in which case the impacting particle density could have been  $1 \text{ g cm}^{-3}$ . The particle core is consistent with 1.9 pg forsterite ( $3.3 \text{ g cm}^{-3}$ ): the area of the core region was  $0.85 \pm 0.15 \mu\text{m}^2$  (from a 40 nm pixel 875 eV image), equivalent to  $0.6 \mu\text{m}^3$ . Assuming that the particle was  $2 \mu\text{m}$  in diameter on impact, and that the outer particle was comprised of metal oxides, the density of metal oxides would have been  $1.5 \text{ g cm}^{-3}$ . These porous fine-grained phases distributed into the aerogel on capture, forming a lower density halo.

We found clear evidence that the documented overexposure at ID13 resulted in 50% amorphization of forsterite, but we did not find evidence of any mass loss of Fe to the surrounding aerogel (cf. Track 30). The combined dose history experienced during the XRF, XRD, and STXM analyses by the particles in Track 34 is shown in Fig. 26.

### **I1003,1,40 (Track 40, Sorok)**

Track 40 is a very large track, whose morphology is consistent with very high-speed ( $>15 \text{ km s}^{-1}$ ) capture (Postberg et al. 2014). Track 40 does not appear in any Stardust@home images; it was discovered when one of us (AJW) was setting up another extraction on Tile I1003, and he named it Sorok. The aerogel density of the  $100 \mu\text{m}$  thick picokeystone was very low, estimated at  $12 \pm 1 \text{ mg cm}^{-3}$  from a 1000 eV image of the picokeystone, which allowed for carbon analysis.

We first collected absorption images of the track and could not identify any obvious terminal particles, although a few small spots were observed with higher than average absorption. We acquired a stack at the C K-edge around 290 eV: in this case, C measurements were limited by our self-imposed photon dose limits, rather than being prevented by the aerogel thickness. We collected 100 nm step maps at the C, O, Mg, Al, and Si K-edges, and at the Fe L-edge with a 40 nm step size. In Fig. 27, we show elemental maps of Sorok. From these images, we measured the track mouth to be  $14 \mu\text{m}$  in diameter, and the bulb dimensions were  $19 \mu\text{m}$  wide and  $29 \mu\text{m}$  long (in the direction of impact).

It appears that the original projectile in Track 40 was almost entirely destroyed during high-speed capture. The 2-dimensional track area of  $500 \mu\text{m}^2$  would result in a 3 pg impactor (like Track 30) having a total column density distribution of  $6 \text{ fg } \mu\text{m}^{-2}$ , which is

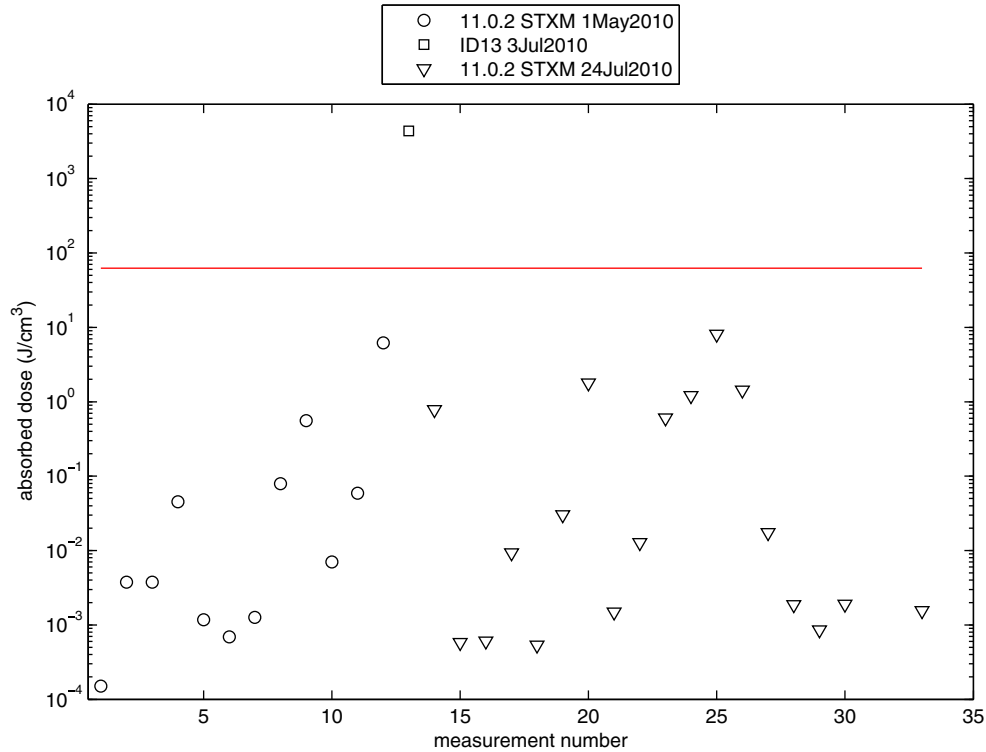


Fig. 26. Analytical X-ray absorbed dose for analyses of Hylabrook, versus analysis sequence. We plot individual STXM analyses (circles, triangles) and summed SXRF/SXRD analyses at ID13 at European synchrotron radiation facility (ESRF) (square). The horizontal line is the ISPE self-imposed limit based on expected interstellar irradiation (Gruber et al. 1999).

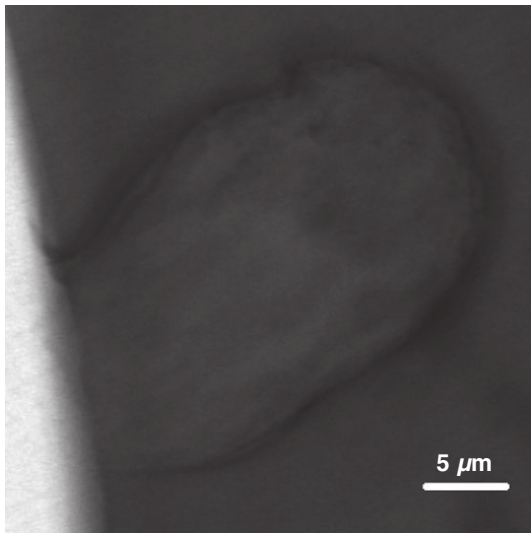


Fig. 27. 705 eV absorption image of Track 40 showing a 29  $\mu\text{m}$  long crater-shaped track with 14  $\mu\text{m}$  mouth diameter.

around the detection limit for many elements in STXM. We can probably rule out Sorok being an Fe-rich particle like Orion or Hylabrook, because we would expect to detect approximately  $2 \text{ fg } \mu\text{m}^{-2}$  of Fe

(equivalent to 1 pg total mass of Fe). Carbon sensitivity of STXM is high, but the high C background in aerogel limits interpretation of C analyses. In addition, capture effects of carbon phases in hypervelocity impacts into aerogel are not well understood, so our C XANES was inconclusive. Analysis of the Track 40 residues, if any survived, may depend on new instruments currently under development (e.g., Stephan et al. 2012).

## CONCLUSIONS

The goal of the ISPE STXM analyses was to refine the list of impact features identified through the Stardust@home distributed search (Westphal et al. 2014a) and extracted at NASA Johnson Space Center, Houston (Frank et al. 2013) to identify the most likely interstellar candidates. We developed efficient procedures to differentiate spacecraft contaminants originating from secondary impacts and terrestrial manufacturing contaminants, from extraterrestrial primary impacts. We confirmed the association of impact particles and tracks using high-resolution absorption imaging ( $X$ - $Y$  spatial resolution up to 15 nm, depth resolution 2  $\mu\text{m}$  at 800 eV), and characterized the major element chemistry of impactors.

We rejected nine midnight tracks, whose trajectories were consistent with either interstellar dust or the SRC Deck. Six of the midnight track impacts comprised Al metal, distinguishable by Al XANES, and we rejected two other impactors from the same trajectory population containing amorphous Al oxide, which matched Al XANES spectra of SRC deck material. The presence of Al in oxidized and not metallic form was not sufficient reason to reject these candidates. However, we detected fluorine in Track 37 (Merlin) and in a carbon-rich region of anodized SRC deck (Frank et al. 2013), which indicates a plausible spacecraft origin for this particle. Flynn et al. (2014) reported that Track 2, the second Al-oxide impactor, was unlikely to have an extraterrestrial origin based on the relative concentrations of its heavy elements. We also rejected Track 28, which probably originated from Mylar film present on the SRC deck. The tenth midnight track, Track 38, was too thick for STXM analysis; no other techniques have yet been applied and the origin of that impactor remains unknown.

We rejected four impacts based on their high abundance of cosmochemically rare Ce, a known component of spacecraft solar glass panel covers. These impacts had a trajectory consistent with an aft solar panel origin.

We rejected 12 features including terrestrial surface contaminants and backgrounds from aerogel manufacture. In STXM images, none of these samples showed evidence of high-speed impact origin.

The large population of tracks visible in Tile I1029 with trajectory about 90° from the interstellar dust stream (“9 o’clock swarm”) were not considered interstellar candidates, based on their trajectory and high abundance. We found evidence for some surviving impactor material, most likely of extraterrestrial, solar system origin, including Mg-rich silicate phases and corundum.

Three plausible candidates remain, which we could not reject based on their chemical characterizations. For two of these, the STXM analyses were carried out in coordination with XRF and XRD analyses. The terminal particle in Track 30 (Orion) was originally a 3 pg,  $0.7 \text{ g cm}^{-3}$  object comprising forsterite, a medium-range ordered phase with Mg-spinel composition, a fraction of crystalline spinel, plus an iron phase. Track 34 (Hylabrook) was a 4 pg particle with a 1.9 pg olivine core surrounded by a low-density (approximately  $1 \text{ g cm}^{-3}$ ), fine-grained halo, including amorphous Mg-silicate, and amorphous Fe, Cr, Mn, Al, Ca phases. Track 40 (Sorok) has the track morphology of a high-speed impact, but contained no detectable residue that was convincingly distinguishable from the background aerogel.

Comparisons of impact track morphology in aerogel with collection speed (Postberg et al. 2014) suggest that the impact speeds of Tracks 30 and 34 could have been as low as  $2 \text{ km s}^{-1}$ . We found no evidence for spacecraft secondary ejecta in Tracks 30 and 34, suggesting that these were primary impacts. Postberg et al. (2014) concluded that the probable impact speed of the projectile that formed Track 40 (Sorok) was  $>10 \text{ km s}^{-1}$ . The high-speed impact is consistent with the lack of a terminal particle. The range of impact speeds of incoming interstellar dust to the Stardust IS collector (Sterken et al. 2014) is related to mass and particle morphology. Orion and Hylabrook were consistent with the high-mass, low-speed tail of the modeled dust distribution by Sterken et al. (2014); Sorok was consistent with high-speed, fluffy particles.

Because of the rarity of interstellar grain candidates in the SIDC, we performed deliberately limited analyses on them. We found no evidence of radiation damage to any of the SIDC samples caused by STXM. FTIR measurements of carbon in picokeystones before and after STXM analyses found no change (Bechtel et al. 2014). We did encounter unexpected problems with some hard X-ray XRF/XRD analyses, possibly exacerbated by the aerogel capture medium (Simionovici et al. 2014). Here, we used STXM to track the changes to both particles and aerogel. STXM has proven to be a powerful, versatile analytical tool for analysis of impact features extracted from the SIDC aerogel collectors. STXM is uniquely capable of performing high spatial resolution mapping and spectroscopy of C, Mg, Al, Si, Fe, and Ni in particles and impact features in situ in the Stardust aerogel capture media.

*Acknowledgments*—The ISPE consortium gratefully acknowledges the NASA Discovery Program for Stardust, the fourth NASA Discovery mission. AJW, ALB, ZG, RL, DZ, WM, and JVK were supported by NASA grant NNX09AC36G. RMS, HCG, and NDB were supported by NASA grant NNN11AQ61I. The ALS is supported by the Director, Office of Science, Office of Basic Energy Sciences, of the U.S. Department of Energy, under Contract No. DE-AC02-05CH11231. Use of the National Synchrotron Light Source, Brookhaven National Laboratory, was supported by the U.S. Department of Energy, Office of Science, Office of Basic Energy Sciences, under Contract No. DE-AC02-98CH10886. We appreciate greatly the thorough reviews by one anonymous reviewer, John Bradley, and associate editor, Christian Koeberl. Their contributions improved the manuscript and helped to clarify key findings. We thank Steve Boggs for helpful discussions regarding X-ray dose estimates in the Interstellar



Medium, and for providing diffuse X-ray data. We thank the Natural History Museum, London, for providing most of the standards used for acquiring the XANES spectra library in this work.

## REFERENCES

- Bechtel H. A., Flynn G., Allen C., Anderson D., Ansari A., Bajt S., Bastien R. K., Bassim N., Borg J., Brenker F. E., Bridges J., Brownlee D. E., Burchell M., Burghammer M., Butterworth A. L., Changela H., Cloetens P., Davis A. M., Doll R., Floss C., Frank D., Gainsforth Z., Grün E., Heck P. R., Hillier J. K., Hoppe P., Hudson B., Huth J., Hvide B., Kearsley A., King A. J., Lai B., Leitner J., Lemelle L., Leroux H., Leonard A., Lettieri R., Marchant W., Nittler L. R., Ogliore R., Ong W. J., Postberg F., Price M. C., Sandford S. A., Tresseras J. S., Schmitz S., Schoonjans T., Silversmit G., Simionovici A. S., Solé V. A., Srama R., Stephan T., Sterken V. J., Stodolna J., Stroud R. M., Sutton S., Trieloff M., Tsou P., Tsuchiyama A., Tyliczszak T., Vekemans B., Vincze L., Korff J. V., Westphal A. J., Wordsworth N., Zevin D., Zolensky M. E., and > 30,000 Stardust@home dusters. 2014. Stardust Interstellar Preliminary Examination III: Infrared spectroscopic analysis of interstellar dust candidates. *Meteoritics & Planetary Science*, doi:10.1111/maps.12125.
- Brenker F. E., Schoonjans T., Silversmit G., Vekemans B., Vincze L., Westphal A. J., Allen C., Anderson D., Ansari A., Bajt S., Bastien R. K., Bassim N., Bechtel H. A., Borg J., Bridges J., Brownlee D. E., Burchell M., Burghammer M., Butterworth A. L., Changela H., Cloetens P., Davis A. M., Doll R., Floss C., Flynn G., Fougeray P., Frank D. R., Gainsforth Z., Grün E., Heck P. R., Hillier J. K., Hoppe P., Hudson B., Huth J., Hvide B., Kearsley A., King A. J., Lai B., Leitner J., Lemelle L., Leroux H., Leonard A., Lettieri R., Marchant W., Nittler L. R., Ogliore R., Ong W. J., Postberg F., Price M. C., Sandford S. A., Sans Tresseras J., Schmitz S., Simionovici A. S., Solé V. A., Srama R., Stadermann F., Stephan T., Sterken V. J., Stodolna J., Stroud R. M., Sutton S., Trieloff M., Tsou P., Tsuchiyama A., Tyliczszak T., Korff J. V., Wordsworth N., Zevin D., Zolensky M. E., and > 30,000 Stardust@home dusters. 2014. Stardust Interstellar Preliminary Examination V: XRF analyses of interstellar dust candidates at ESRF ID13. *Meteoritics & Planetary Science*, doi:10.1111/maps.12206.
- Butterworth A. L., Tyliczszak T., Gainsforth Z., Ogliore R., Snead C. J., and Westphal A. J. 2008. Scanning transmission X-ray microscopy as a tool for analysis of interstellar dust captured in aerogel (abstract #2283). 39th Lunar and Planetary Science Conference. CD-ROM.
- Cabaret D., Saintavit P., Ildefonse P., and Flank A. 1998. Full multiple scattering calculations of the X-ray absorption near edge structure at the magnesium K-edge in pyroxene. *American Mineralogist* 83:300–304.
- Flynn G., Sutton S., Lai B., Wirick S., Allen C., Anderson D., Ansari A., Bajt S., Bastien R. K., Bassim N., Bechtel H. A., Borg J., Brenker F. E., Bridges J., Brownlee D. E., Burchell M., Burghammer M., Butterworth A. L., Changela H., Cloetens P., Davis A. M., Doll R., Floss C., Frank D. R., Gainsforth Z., Grün E., Heck P. R., Hillier J. K., Hoppe P., Hudson B., Huth J., Hvide B., Kearsley A., King A. J., Leitner J., Lemelle L., Leroux H., Leonard A., Lettieri R., Marchant W., Nittler L. R., Ogliore R., Ong W. J., Postberg F., Price M. C., Sandford S. A., Srama R., Stephan T., Sterken V. J., Stodolna J., Stroud R. M., Sutton S., Trieloff M., Tsou P., Tsuchiyama A., Tyliczszak T., Vekemans B., Vincze L., Korff J. V., Wordsworth N., Zevin D., Zolensky M. E., and > 30,000 Stardust@home dusters. 2014. Stardust Interstellar Preliminary Examination VII: Synchrotron X-ray fluorescence analysis of six Stardust interstellar candidates measured with the advanced photon source 2-ID-D microprobe. *Meteoritics & Planetary Science*, doi:10.1111/maps.12144.
- Frank D. R., Westphal A. J., Zolensky M. E., Bastien R. K., Gainsforth Z., Allen C., Anderson D., Ansari A., Bajt S., Bassim N., Bechtel H. A., Borg J., Brenker F. E., Bridges J., Brownlee D. E., Burchell M., Burghammer M., Butterworth A. L., Changela H., Cloetens P., Davis A. M., Doll R., Floss C., Flynn G., Grün E., Heck P. R., Hillier J. K., Hoppe P., Hudson B., Huth J., Hvide B., Kearsley A., King A. J., Lai B., Leitner J., Lemelle L., Leroux H., Leonard A., Lettieri R., Marchant W., Nittler L. R., Ogliore R., Ong W. J., Postberg F., Price M. C., Sandford S. A., Tresseras J. S., Schmitz S., Schoonjans T., Silversmit G., Simionovici A. S., Solé V. A., Srama R., Stephan T., Sterken V. J., Stodolna J., Stroud R. M., Sutton S., Trieloff M., Tsou P., Tsuchiyama A., Tyliczszak T., Vekemans B., Vincze L., Korff J. V., Wordsworth N., Zevin D., and > 30,000 Stardust@home dusters. 2013. Stardust Interstellar Preliminary Examination II: Curating the interstellar dust collector, picokeystones, and sources of impact tracks. *Meteoritics & Planetary Science*, doi:10.1111/maps.12147.
- Gainsforth Z., Brenker F. E., Burghammer M., Simionovici A. S., Schmitz S., Cloetens P., Lemelle L., Sans Tresseras J., Schoonjans T., Silversmit G., Solé V. A., Vekemans B., Vincze L., Westphal A. J., Allen C., Anderson D., Ansari A., Bajt S., Bastien R. K., Bassim N., Bechtel H. A., Borg J., Bridges J., Brownlee D. E., Burchell M., Butterworth A. L., Changela H., Davis A. M., Doll R., Floss C., Flynn G., Frank D. R., Grün E., Heck P. R., Hillier J. K., Hoppe P., Hudson B., Huth J., Hvide B., Kearsley A., King A. J., Lai B., Leitner J., Leroux H., Leonard A., Lettieri R., Marchant W., Nittler L. R., Ogliore R., Ong W. J., Postberg F., Price M. C., Sandford S. A., Srama R., Stephan T., Sterken V. J., Stodolna J., Stroud R. M., Sutton S., Trieloff M., Tsou P., Tsuchiyama A., Tyliczszak T., Korff J. V., Wordsworth N., Zevin D., Zolensky M. E., and > 30,000 Stardust@home dusters. 2014. Stardust Interstellar Preliminary Examination VIII: Identification of crystalline material in two interstellar candidates. *Meteoritics & Planetary Science*, doi:10.1111/maps.12148.
- Gruber D. E., Matteson J. L., Peterson L. E., and Jung G. V. 1999. The spectrum of diffuse cosmic hard X-rays measured with HEAO 1. *The Astrophysical Journal* 520:124–129.
- Ildefonse P., Cabaret D., Saintavit P., and Calas G. 1998. Aluminium X-ray absorption near edge structure in model compounds and earth's surface minerals. *Physics and Chemistry of Minerals* 25:112–121.
- Ildefonse P., Calas G., Flank A. M., and Lagarde P. 1995. Low Z elements (Mg, Al, and Si) K-edge X-ray absorption spectroscopy in minerals and disordered systems. *Nuclear Instruments and Methods in Physics Research Section B: Beam Interactions with Materials and Atoms* 97:172–175.

- Jacobsen C., Flynn G., Wirick S., and Zimba C. 2000. Soft X-ray spectroscopy from image sequences with sub-100 nm spatial resolution. *Journal of Microscopy* 197:173–184.
- Jones A. P., Tielens A. G. G. M., and Hollenbach D. J. 1996. Grain shattering in shocks: The interstellar grain size distribution. *The Astrophysical Journal* 469:740.
- Kilcoyne A. L. D. and Tylliszczak T. 2004. Fast soft X-ray beam shutter. *AIP Conference Proceedings* 705:605.
- Lerotic M., Jacobsen C., Gillow J. B., Francis A. J., Wirick S., Vogt S., and Maser J. 2005. Cluster analysis in soft X-ray spectromicroscopy: Finding the patterns in complex specimens. *Journal of Electron Spectroscopy and Related Phenomena* 144–147:1137–1143.
- Li D., Bancroft G. M., Fleet M. E., Feng X. H., and Pan Y. 1995. Al K-edge XANES spectra of aluminosilicate minerals. *American Mineralogist* 80:432–440.
- Li D., Peng M., and Murata T. 1999. Coordination and local structure of magnesium in silicate minerals and glasses; Mg K-edge XANES study. *The Canadian Mineralogist* 37:199–206.
- Marcelli A., Mottana A., and Cibin G. 2000. Next-neighbour interactions with Al in Li +- and Rb +-exchanged Na +B-aluminas, detected by synchrotron X-ray absorption spectroscopy. *Journal of Applied Crystallography* 33:234–242.
- Mottana A., Murata T., Marcelli A., Ventura Della G., Cibin G., Wu Z., and Tessadri R. 1998. Characterization of local chemistry and disorder in synthetic and natural  $\alpha$ -Al<sub>2</sub>O<sub>3</sub> materials by X-ray absorption near-edge structure spectroscopy. *Journal of Applied Crystallography* 31:890–898.
- Neuvill D. R., Ligny D. D., Cormier L., Henderson G. S., Roux J., Flank A., and Lagarde P. 2009. The crystal and melt structure of spinel and alumina at high temperature: An in-Situ XANES study at the Al and Mg K-edge. *Geochimica et Cosmochimica Acta* 73:3410–3422.
- Olynick D. L., Harteneck B. D., Veklerov E., Tendulkar M., Liddle J. A., Kilcoyne A. L. D., and Tylliszczak T. 2004. 25 nm mechanically buttressed high aspect ratio zone plate fabrication and performance. *Journal of Vacuum Science Technology* B22:3186–3190.
- Postberg F., Hillier J. K., Armes S. P., Bugiel S., Butterworth A. L., Dupin D., Fielding L. A., Fujii S., Gainsforth Z., Grün E., Li Y. W., Srama R., Sterken V. J., Stodolna J., Trieloff M., Westphal A. J., Allen C., Anderson D., Ansari A., Bajt S., Bastien R. K., Bassim N., Bechtel H. A., Borg J., Brenker F. E., Bridges J., Brownlee D. E., Burchell M., Burghammer M., Changela H., Cloetens P., Davis A. M., Doll R., Floss C., Flynn G., Frank D. R., Heck P. R., Hoppe P., Hudson B., Huth J., Hvide B., Kearsley A., King A. J., Lai B., Leitner J., Lemelle L., Leroux H., Leonard A., Lettieri R., Marchant W., Nittler L. R., Ogliore R., Ong W. J., Price M. C., Sandford S. A., Tresseras J. S., Schmitz S., Schoonjans T., Silversmit G., Simionovici A., Solé V. A., Stephan T., Stroud R. M., Sutton S., Tsou P., Tsuchiyama A., Tylliszczak T., Vekemans B., Vincze L., Korff J. V., Wordsworth N., Zevin D., Zolensky M. E., and >30,000 Stardust@home dusters. 2014. Stardust Interstellar Preliminary Examination IX: High speed interstellar dust analogue capture in Stardust flight-spare aerogel. *Meteoritics & Planetary Science*, doi:10.1111/maps.12173.
- Simionovici A. S., Lemelle L., Cloetens P., Solé V. A., Sans Tresseras J., Butterworth A. L., Westphal A. J., Gainsforth Z., Stodolna J., Allen C., Anderson D., Ansari A., Bajt S., Bassim N., Bastien R. K., Bechtel H. A., Borg J., Brenker F. E., Bridges J., Brownlee D. E., Burchell M., Burghammer M., Changela H., Davis A. M., Doll R., Floss C., Flynn G., Frank D. R., Grün E., Heck P. R., Hillier J. K., Hoppe P., Hudson B., Huth J., Hvide B., Kearsley A., King A. J., Lai B., Leitner J., Leonard A., Lettieri R., Marchant W., Nittler L. R., Ogliore R., Ong W. J., Price M. C., Sandford S. A., Tresseras J. S., Schmitz S., Schoonjans T., Silversmit G., Simionovici A., Solé V. A., Stephan T., Stroud R. M., Sutton S., Tsou P., Tsuchiyama A., Tylliszczak T., Vekemans B., Vincze L., Korff J. V., Wordsworth N., Zevin D., Zolensky M. E., and >30,000 Stardust@home dusters. 2014. Stardust Interstellar Preliminary Examination VI: Quantitative elemental analysis by synchrotron X-ray fluorescence nanoimaging of eight impact features in aerogel. *Meteoritics & Planetary Science*, doi:10.1111/maps.12208.
- Stephan T., Davis A. M., Pellin M. J., Savina M. R., Trappitsch R., Rost D., King A. J., Liu N., and Yokochi R. 2012. Analyzing stardust with CHILI—The Chicago instrument for laser ionization (abstract). *Meteoritics & Planetary Science* 47 (Suppl.):5290.
- Sterken V. J., Westphal A. J., Altobelli N., Grün E., Hillier J. K., Postberg F., Srama R., Allen C., Anderson D., Ansari A., Bajt S., Bastien R. K., Bassim N., Bechtel H. A., Borg J., Brenker F. E., Bridges J., Brownlee D. E., Burchell M., Burghammer M., Butterworth A. L., Changela H., Cloetens P., Davis A. M., Doll R., Floss C., Flynn G., Frank D., Gainsforth Z., Heck P. R., Hoppe P., Hudson B., Huth J., Hvide B., Kearsley A., King A. J., Lai B., Leitner J., Lemelle L., Leroux H., Leonard A., Lettieri R., Marchant W., Nittler L. R., Ogliore R., Ong W. J., Price M. C., Sandford S. A., Tresseras J. S., Schmitz S., Schoonjans T., Silversmit G., Simionovici A., Solé V. A., Stadermann F., Stephan T., Stodolna J., Stroud R. M., Sutton S., Trieloff M., Tsou P., Tsuchiyama A., Tylliszczak T., Vekemans B., Vincze L., Korff J. V., Wordsworth N., Zevin D., Zolensky M. E., and >30,000 Stardust@home dusters. 2014. Stardust Interstellar Preliminary Examination X: Impact speeds and directions of interstellar grains on the Stardust dust collector. *Meteoritics & Planetary Science*, doi:10.1111/maps.12219.
- Stroud R. M., Allen C., Anderson D., Ansari A., Bajt S., Bassim N., Bastien R. K., Bechtel H. A., Borg J., Brenker F. E., Bridges J., Brownlee D. E., Burchell M., Burghammer M., Butterworth A. L., Changela H., Cloetens P., Davis A. M., Doll R., Floss C., Flynn G., Frank D. R., Gainsforth Z., Grün E., Heck P. R., Hillier J. K., Hoppe P., Huth J., Hvide B., Kearsley A., King A. J., Lai B., Leitner J., Lemelle L., Leroux H., Leonard A., Lettieri R., Marchant W., Nittler L. R., Ogliore R., Ong W. J., Postberg F., Price M. C., Sandford S. A., Sans Tresseras J., Schmitz S., Schoonjans T., Silversmit G., Simionovici A. S., Solé V. A., Srama R., Stephan T., Sterken V. J., Stodolna J., Sutton S., Trieloff M., Tsou P., Tsuchiyama A., Tylliszczak T., Vekemans B., Vincze L., Korff J. V., Westphal A. J., and Zevin D. 2014. Stardust Preliminary Examination XI: Identification and elemental analysis of impact craters on Al foils from the Stardust Interstellar Dust Collector. *Meteoritics & Planetary Science*, doi:10.1111/maps.12136.

- Thompson S. P. 2008. Structural signatures of medium-range order in annealed laboratory silicates. *Astronomy & Astrophysics* 484:251–265.
- Tyliszczak T., Warwick T., Kilcoyne A. L. D., Fakra S., Shuh D. K., Yoon T. H., Brown G. E., Andrews S., Chembrolu V., Strachan J., and Acremann Y. 2004. Soft X-ray scanning transmission microscope working in an extended energy range at the Advanced Light Source. *Eighth International Conference on Synchrotron Radiation Instrumentation, AIP Conference Proceedings* 705:1356–1359.
- Wang J., Morin C., Li L., Hitchcock A. P., Scholl A., and Doran A. 2009. Radiation damage in soft X-ray microscopy. *Journal of Electron Spectroscopy and Related Phenomena* 170:25–36.
- Westphal A. J., Snead C. J., Butterworth A. L., Graham G. A., Bradley J. P., Bajt S., Grant P. G., Bench G., Brennan S., and Pianetta P. 2004. Aerogel keystones: Extraction of complete hypervelocity impact events from aerogel collectors. *Meteoritics & Planetary Science* 39:1375–1386.
- Westphal A. J., Bechtel H. A., Brenker F. E., Butterworth A. L., Flynn G., Frank D. R., Gainsforth Z., Hillier J. K., Postberg F., Simionovici A. S., Sterken V. J., Stroud R. M., Allen C., Anderson D., Ansari A., Bajt S., Bastien R. K., Bassim N., Borg J., Bridges J., Brownlee D. E., Burchell M., Burghammer M., Changela H., Cloetens P., Davis A. M., Doll R., Floss C., Grün E., Heck P. R., Hoppe P., Hudson B., Huth J., Hvide B., Kearsley A., King A. J., Lai B., Leitner J., Lemelle L., Leroux H., Leonard A., Lettieri R., Marchant W., Nittler L. R., Ogliore R., Ong W. J., Price M. C., Sandford S. A., Sans Tresseras J., Schmitz S., Schoonjans T., Silversmit G., Solé V. A., Srama R., Stadermann F., Stephan T., Stodolna J., Sutton S., Tieloff M., Tsou P., Tsuchiyama A., Tyliszczak T., Vekemans B., Vincze L., Korff J. V., Wordsworth N., Zevin D., Zolensky M. E., and > 30,000 Stardust@home dusters. 2014a. Final reports of the Stardust Interstellar Preliminary Examination. *Meteoritics & Planetary Science*, doi:10.1111/maps.12221.
- Westphal A. J., Anderson D., Butterworth A. L., Frank D. R., Hudson B., Lettieri R., Marchant W., Korff J. V., Zevin D., Ardizzone A., Campanile A., Capraro M., Courtney K., Crumpler D., Cwik R., Gray F. J., Imada G., Karr J., Lau Wan Wah L., Mazzucato M., Motta P. G., Spencer R. C., Woodrough S. B., Santoni I. C., Sperry G., Terry J., Wordsworth N., Yanke T., Sr., Allen C., Ansari A., Bajt S., Bastien R. K., Bassim N., Bechtel H. A., Borg J., Brenker F. E., Bridges J., Brownlee D. E., Burchell M., Burghammer M., Changela H., Cloetens P., Davis A. M., Doll R., Floss C., Flynn G., Gainsforth Z., Grün E., Heck P. R., Hillier J. K., Hoppe P., Huth J., Hvide B., Kearsley A., King A. J., Lai B., Leitner J., Lemelle L., Leroux H., Leonard A., Nittler L. R., Ogliore R., Ong W. J., Postberg F., Price M. C., Sandford S. A., Tresseras J. S., Schmitz S., Schoonjans T., Silversmit G., Simionovici A. S., Solé V. A., Srama R., Stadermann F., Stephan T., Sterken V. J., Stodolna J., Stroud R. M., Sutton S., Tieloff M., Tsou P., Tsuchiyama A., Tyliszczak T., Vekemans B., Vincze L., Zolensky M. E., and > 30,000 Stardust@home dusters. 2014b. Stardust Interstellar Preliminary Examination I: Identification of tracks in aerogel. *Meteoritics & Planetary Science*, doi:10.1111/maps.12168.
- Wozniakiewicz P. J., Kearsley A. T., Burchell M. J., Foster N. J., Cole M. J., Bland P. A., and Russell S. S. 2009. In situ analysis of residues resulting from laboratory impacts into aluminum 1100 foil: Implications for Stardust crater analyses. *Meteoritics & Planetary Science* 44:1541–1559.
- Wu Z., Mottana A., Marcelli A., and Natoli C. R. 1996. Theoretical analysis of X-ray absorption near-edge structure in forsterite,  $\text{Mg}_2\text{SiO}_4$ -Pbnm, and fayalite,  $\text{Fe}_2\text{SiO}_4$ -Pbnm, at room temperature and extreme conditions. *Physics and Chemistry of Minerals* 23:193–204.